Computational Schemes for Flexible, Nonlinear Multi-Body Systems *

Olivier A. Bauchau
Georgia Institute of Technology, School of Aerospace Engineering
Atlanta, GA, USA

Abstract

This paper deals with the development of computational schemes for the dynamic analysis of flexible, nonlinear multi-body systems. The focus of the investigation is on the derivation of unconditionally stable time integration schemes for these types of problem. At first, schemes based on Galerkin and time discontinuous Galerkin approximations applied to the equations of motion written in the symmetric hyperbolic form are proposed. Though useful, these schemes require casting the equations of motion in the symmetric hyperbolic form, which is not always possible for multi-body applications. Next, unconditionally stable schemes are proposed that do not rely on the symmetric hyperbolic form. Both energy preserving and energy decaying schemes are derived that both provide unconditionally stable schemes for nonlinear multi-body systems. The formulation of beam and flexible joint elements, as well as of the kinematic constraints associated with universal and revolute joints. An automated time step selection procedure is also developed based on an energy related error measure that provides both local and global error levels. Several examples of simulation of realistic multi-body systems are presented which illustrate the efficiency and accuracy of the proposed schemes, and demonstrate the need for unconditional stability and high frequency numerical dissipation.

1 Introduction

This paper is concerned with the dynamic analysis of flexible, nonlinear multi-body systems, *i.e.* a collection of bodies in arbitrary motion with respect to each other while each body is undergoing large displacements and rotations with respect to a body attached frame of reference. The focus is on problems where the strains within each elastic body remain small.

The elastic bodies are modeled using the finite element method. The use of beam and flexible joint elements will be demonstrated for multi-body systems. The location of each node is represented by its Cartesian coordinates in an inertial frame, and the rotation of the cross-section at each node is represented by a finite rotation tensor expressed in the same

* *Multibody System Dynamics*, **2**, 1998, pp 169-225.

inertial frame. The kinematic constraints among the various bodies are enforced via the Lagrange multiplier technique. Although this approach does not involve the minimum set of coordinates, it allows a modular development of finite elements for the enforcement of the kinematic constraints. The formulation of universal and revolute joints will be presented here.

The equations of motion resulting from the modeling of multi-body systems with the above methodology present distinguishing features: they are stiff, nonlinear, differential-algebraic equations. The stiffness of the system stems from the presence of high frequencies in the elastic members, but also from the infinite frequencies associated with the kinematic constraints. Indeed, no mass is associated with the Lagrange multipliers giving rise to algebraic equations coupled to the other equations of the system which are differential in nature.

This paper is concerned with the time integration of the equations of motion describing the nonlinear dynamic response of multi-body systems. The main focus is on the derivation of an algorithm presenting high frequency numerical dissipation, and for which unconditional stability can be proven in the nonlinear case. An energy decay argument will be used to establish stability [1].

The Newmark algorithm [2] is widely used in structural dynamics. In particular, the average acceleration method, also known as the trapezoidal rule, is an unconditionally stable, second order accurate scheme when applied to linear problems. The classical stability analysis of this scheme can be readily found in text books [3] and shows that the spectral radius remains exactly equal to unity at all frequencies. An alternate way of proving stability is based on an energy argument. Indeed, it is easily shown that the average acceleration scheme exactly preserves the total energy of the system [1].

For large finite element discretizations very high frequencies are present in the model and high frequency numerical dissipation is desirable, if not indispensable. Numerical dissipation cannot be introduced in the Newmark method without degrading the accuracy. Hilber, Hughes, and Taylor [4] introduced the α-method to remedy this situation. More recently, the generalized-α method [5] was introduced that achieves high frequency dissipation while minimizing unwanted low frequency dissipation. Both methods have been successfully used for both linear and nonlinear problems, though unconditional stability is proved for linear systems only.

Simo and his co-workers presented energy preserving schemes for rigid body dynamics [6], elasto-dynamics [7], and beams [8]. The unconditional stability of these schemes stems from a proof of preservation of the total energy of the system. An energy preserving scheme for nonlinear elastic multi-body systems was proposed by Bauchau [9]. In this scheme, the equations of motion are discretized so that they imply conservation of the total energy for the elastic components of the system, whereas the forces of constraint associated with the kinematic constraints are discretized so that the work they perform vanishes exactly. The combination of these two features of the discretization guarantees the stability of the numerical integration process for nonlinear elastic multi-body systems.

Though energy preserving schemes perform well, their lack of high frequency numerical dissipation can be a problem [9]. First, the time histories of internal forces and velocities can present a very significant high frequency content. Second, it seems that the presence of high frequency oscillations can hinder the convergence process for the solution of the

nonlinear equations of motion. This was observed in several examples where the dynamic response of the system does involve significant high frequency content. The selection of a smaller time step does not necessarily help this convergence process, as a smaller time step allows even higher frequency oscillations to be present in the response. Finally, it seems that the presence of high frequency oscillations also renders strict energy preservation difficult to obtain. This could prove to be a real limitation of energy preserving schemes when applied to more and more complex models. For such models, the use of integration schemes presenting high frequency numerical dissipation become increasingly desirable.

It appears that the development of "energy decaying" schemes, *i.e.* schemes eliminating the energy associated with vibratory motions at high frequency, is desirable. This is particularly important when dealing with problems presenting a complex dynamic response such as constrained flexible multi-body problems.

The key to the development of an energy decaying scheme is the derivation of an *energy decay inequality* [1] rather that the *discrete energy conservation law* which is central to energy preserving schemes. A methodology that can systematically lead to an energy decay inequality is the *time discontinuous Galerkin method* [10, 11, 12] which was initially developed for hyperbolic equations. Hughes and Hulbert [13, 14] have investigated the use of the time discontinuous Galerkin methodology for linear elasto-dynamics. They point out that

> classical elasto-dynamics can be converted to first-order symmetric hyperbolic form, which has proved useful in theoretical studies. Finite element methods for first order symmetric hyperbolic system are thus immediately applicable. However, there seems to be several disadvantages: in symmetric hyperbolic form the state vector consists of displacements, velocities, and stresses which is computationally uneconomical; and the generalization to nonlinear elasto-dynamics seems possible only in special circumstances.

Indeed, writing the nonlinear equations of motion of beams in this symmetric hyperbolic form does not appear to be possible.

In this paper an alternate route is taken. Practical time integration schemes that do not rely on the symmetric hyperbolic form of the equations of motion are developed. These schemes are of a finite difference nature, and imply an energy balance condition that is obtained by a direct computation of the work done by the discretized inertial and elastic forces over a time step. The mean value theorem guarantees the existence of discretizations leading to these energy preservation of energy decay statements providing a rigorous proof of unconditional stability for the scheme.

Energy decaying schemes were presented by Bauchau and his co-workers for beams [15], elasto-dynamics [16], and multi-body systems [17]. Bottasso and Borri proposed both energy preserving and decaying schemes for beams [18, 19] and multi-body systems [20, 21].

The first part of this paper describes the theoretical background of the proposed methodology and is organized in the following manner. In section 2, the symmetric hyperbolic form of the equations of motions will be discussed, and the properties of both Galerkin and time discontinuous Galerkin approximations of these equations written in the symmetric hyperbolic form will be presented. Practical time integration schemes that bypass the need for recasting the equations of motion in the symmetric hyperbolic form will then be introduced in section 3. The treatment of constraint equations will be discussed in section 4.

In a second part of the paper, the formulation of a number of elements used in multi-body dynamic analysis will be presented. The discretization of the inertial and elastic forces leading to discrete energy preservation statements will be presented for various elements. The formulation of geometrically exact, shear deformable beam elements, and flexible joint elements will be presented in sections 6.1 and 6.2, respectively. Multi-body systems also involve nonlinear constraints. The formulation of universal and revolute joints will be presented in sections 7.1 and 7.2, respectively.

An important feature of multi-body systems is the rapidly varying nature of their dynamic response. In numerical simulations, it is desirable, and often indispensable to use a variable time step size which value is automatically selected by the analysis software so as to achieve a nearly constant time discretization error as the simulation proceeds. A simple, yet effective time step selection procedure will be presented in section 8. Finally, various numerical simulations of realistic flexible multi-body systems will be presented in section 9.

2 The symmetric hyperbolic form

2.1 Classical forms of the equations of motion

Consider a dynamical system described by a kinetic energy $\mathcal{K} = \mathcal{K}(\dot{u}_p, u_p)$, and a strain energy $\mathcal{V} = \mathcal{V}(u_p)$, where u_p are the degrees of freedom of the system, and $\dot{(.)}$ denotes a derivative with respect to time. The Lagrangian of the system is defined as $\mathcal{L}(\dot{u}_p, u_p) = \mathcal{K} - \mathcal{V}$, and the equations of motion of the system in Lagrangian form are then

$$\frac{d}{dt}\left(\mathcal{L}_{,\dot{u}_p}\right) - \mathcal{L}_{,u_p} = 0. \tag{1}$$

The notation $(.)_{,u}$ is used here to indicate a derivative with respect to u, and a summation is implied by repeated indices. Hamilton's formulation is obtained with the help of a Legendre transformation [22]. First, the momenta are defined as $p_p(\dot{u}_r, u_r) = \mathcal{L}_{,\dot{u}_p}$, and these relationships can be inverted to yield $\dot{u}_p = \dot{u}_p(u_r, p_r)$. The Hamiltonian of the system is now defined

$$\mathcal{H}(u_r, p_r) = p_p \; \dot{u}_p(u_r, p_r) - \mathcal{L}(u_r, p_r). \tag{2}$$

The equations of motion of the system in Hamiltonian form are then

$$\dot{u}_p = \mathcal{H}_{,p_p}; \quad \dot{p}_p + \mathcal{H}_{,u_p} = 0. \tag{3}$$

2.2 The symmetric hyperbolic form

The symmetric hyperbolic form stems from a second Legendre transformation. The following variables are first defined

$$f_p(u_r, p_r) = \mathcal{H}_{,u_p}; \quad v_p(u_r, p_r) = \mathcal{H}_{,p_p}. \tag{4}$$

These relations can be inverted to yield $u_p = u_p(f_r, v_r)$ and $p_p = p_p(f_r, v_r)$. A new function is now defined

$$\mathcal{G}(f_r, v_r) = f_p \; u_p(f_r, v_r) + v_p \; p_p(f_r, v_r) - \mathcal{H}(f_r, v_r), \tag{5}$$

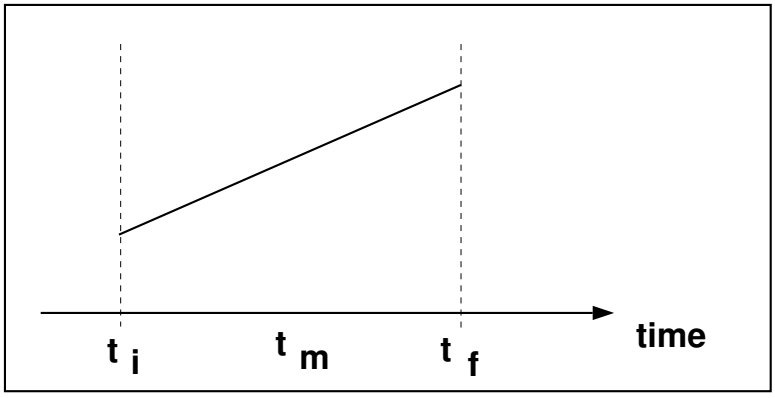

Figure 1: The Galerkin approximation.

implying $u_p = \mathcal{G}_{,f_p}$ and $p_p = \mathcal{G}_{,v_p}$. It can be readily shown that the Hessians of $\mathcal{H}$ and $\mathcal{G}$ are the inverse of each other. Hence, if $\mathcal{H}$ is a definite positive function, so is $\mathcal{G}$. Hamilton's equations (3) can be expressed in terms of the new variables f_p and v_p to find the symmetric hyperbolic form of the equations of motion

$$\mathcal{G}_{,f_p f_q}\ \dot{f}_q + \mathcal{G}_{,f_p v_q}\ \dot{v}_q - v_p = 0; \quad \mathcal{G}_{,v_p f_q}\ \dot{f}_q + \mathcal{G}_{,v_p v_q}\ \dot{v}_q + f_p = 0. \tag{6}$$

To simplify the notation, an implicit form of the equations is preferred

$$\dot{u}_p(f_r, v_r) - v_p = 0; \quad \dot{p}_p(f_r, v_r) + f_p = 0. \tag{7}$$

2.3 The Galerkin approximation

In the Galerkin approximation, the equations of motion are enforced in a weak, integral manner. Fig. 1 shows a time interval from t_i to t_f, and an approximate solution over that interval. Superscripts $(.)^i$ and $(.)^f$ will be used to indicate the value of a quantity at times t_i and t_f, respectively. The Galerkin approximation of the equations of motion in implicit symmetric hyperbolic form (7) writes

$$\int_{t_i}^{t_f} \{w_{1p}[\dot{u}_p(f_r, v_r) - v_p] + w_{2p}[\dot{p}_p(f_r, v_r) + f_p]\}\, dt = 0, \tag{8}$$

where w_{1p} and w_{2p} are arbitrary test functions. Integration by parts yields

$$\int_{t_i}^{t_f} [-\dot{w}_{1p} u_p - \dot{w}_{2p} p_p - w_{1p} v_p + w_{2p} f_p]\, dt + w_{1p}^f u_p^f + w_{2p}^f p_p^f - w_{1p}^i u_p^i - w_{2p}^i p_p^i = 0. \tag{9}$$

This approximation of the equations of motion enjoys remarkable properties. Indeed, selecting the test functions as $w_{1p} = f_p$ and $w_{2p} = v_p$ yields

$$\int_{t_i}^{t_f} [-\dot{f}_p \mathcal{G}_{,f_p} - \dot{v}_p \mathcal{G}_{,v_p} - f_p\ v_p + v_p\ f_p]\ dt + f_p^f\ u_p^f + v_p^f\ p_p^f - f_p^i\ u_p^i - v_p^i\ p_p^i = 0. \tag{10}$$

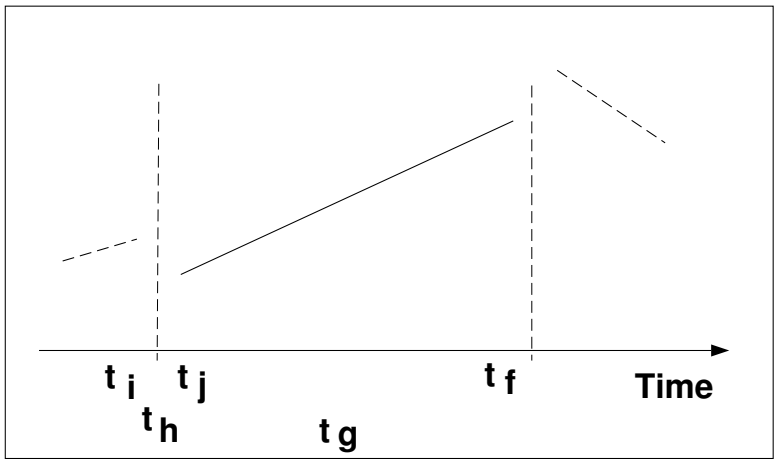

Figure 2: The time discontinuous Galerkin approximation.

The time integral clearly has a closed form solution, leading to

$$\mathcal{G}^i - \mathcal{G}^f + f_p^f \; u_p^f + v_p^f \; p_p^f - f_p^i \; u_p^i - v_p^i \; p_p^i = 0. \tag{11}$$

Finally, we express $\mathcal{G}$ in terms of the Hamiltonian $\mathcal{H}$ with the help of (5) to find

$$\mathcal{H}^f = \mathcal{H}^i. \tag{12}$$

In summary, the Galerkin approximation (8) of the equations of motion written in symmetric hyperbolic form implies a discrete Hamiltonian preservation statement (12). If the Hamiltonian is a definite positive function, this statement implies the *unconditional stability* of integration schemes based on (8).

2.4 The time discontinuous Galerkin approximation

In the time discontinuous Galerkin approximation, the solution is allowed to present discontinuities in the displacement and velocity fields at discrete times. Fig. 2 shows a time interval from t_i to t_f and the approximate solution over that interval. At the initial instant, the solution presents a jump. Superscripts $(.)^i$ will be used to denote the value of a discontinuous quantity on the left side of the jump, whereas a superscript $(.)^j$ indicates the value of that quantity on the right side of the jump. The equations of motion and initial conditions are enforced in a weak, integral manner. The time discontinuous Galerkin approximation of the equations of motion in implicit symmetric hyperbolic form (7) writes

$$\int_{t_j}^{t_f} \{w_{1p}[\dot{u}_p(f_r, v_r) - v_p] + w_{2p}[\dot{p}_p(f_r, v_r) + f_p]\} \, dt + w_{1p}^j \; \langle u_p \rangle + w_{2p}^j \; \langle p_p \rangle = 0. \tag{13}$$

where the notation $\langle . \rangle$ is used to denote the jump in a quantity at the initial time, *i.e.* $\langle u_p \rangle = u_p^j - u_p^i$ and $\langle p_p \rangle = p_p^j - p_p^i$. This approximation of the equations of motion also

enjoys remarkable properties. Indeed, integrating by parts and selecting the test functions as $w_{1p} = f_p$ and $w_{2p} = v_p$ yields

$$\int_{t_j}^{t_f} [-\dot{f}_p \mathcal{G}_{,f_p} - \dot{v}_p \mathcal{G}_{,v_p} - f_p\ v_p + v_p\ f_p]\ dt + f_p^f\ u_p^f + v_p^f\ p_p^f - f_p^j\ u_p^i - v_p^j\ p_p^i = 0. \tag{14}$$

The time integral clearly has a closed form solution, leading to

$$\mathcal{G}^j - \mathcal{G}^f + f_p^f\ u_p^f + v_p^f\ p_p^f - f_p^j\ u_p^i - v_p^j\ p_p^i = 0. \tag{15}$$

Finally, we express $\mathcal{G}$ in terms of the Hamiltonian $\mathcal{H}$ with the help of (5) to find

$$\mathcal{H}^f - \mathcal{H}^j + f_p^j\ \langle u_p \rangle + v_p^j\ \langle p_p \rangle = 0. \tag{16}$$

Since the Hamiltonian is a continuous function of u_r and p_r, the mean value theorem implies

$$\begin{aligned} \mathcal{H}^j = \mathcal{H}^i + f_p^j\ \langle u_p \rangle + v_p^j\ \langle p_p \rangle - \frac{1}{2} \Big[\mathcal{H}^h_{,u_p u_q} \langle u_p \rangle \langle u_q \rangle + \mathcal{H}^h_{,u_p p_q} \langle u_p \rangle \langle p_q \rangle + \\ \mathcal{H}^h_{,p_p u_q} \langle p_p \rangle \langle u_q \rangle + \mathcal{H}^h_{,p_p p_q} \langle p_p \rangle \langle p_q \rangle \Big] = \mathcal{H}^i + f_p^j\ \langle u_p \rangle + v_p^j\ \langle p_p \rangle - c^2, \end{aligned} \tag{17}$$

where the last equality holds if the Hamiltonian is a definite positive function. Combining (16) and (17) then yields

$$\mathcal{H}^f = \mathcal{H}^i - c^2, \Rightarrow \mathcal{H}^f \leq \mathcal{H}^i. \tag{18}$$

In summary, the time discontinuous Galerkin approximation (13) of the equations of motion written in symmetric hyperbolic form implies a Hamiltonian decay inequality (18), if the Hamiltonian is a definite positive quantity. This inequality implies the *unconditional stability* of time integration schemes based on (13).

2.5 Example: Linear spring-mass system

To illustrate the procedures described in the previous sections, a very simple example will be treated here. Consider a linear spring-mass system with a kinetic energy $\mathcal{K} = 1/2\ m\ \dot{u}^2$, a strain energy $\mathcal{V} = 1/2\ k\ u^2$, and subjected to an external force $\mathcal{F}^a(t)$. In this simple case, $f = k\ u$ and $v = p/m$, and the symmetric hyperbolic form of the equations of motion becomes: $\dot{p} + ku = \mathcal{F}^a$; $\quad \dot{u} - p/m = 0$. The Galerkin approximation (8) for this problem writes

$$\int_{t_i}^{t_f} \Big\{ w_1 [\dot{u} - \frac{p}{m}] + w_2 [\dot{p} + ku - \mathcal{F}^a] \Big\}\ dt = 0. \tag{19}$$

Using a linear in time approximation for the displacement and momentum, and a constant in time approximation for the test functions, the following discrete equations are obtained

$$\mathcal{F}^{im} + \mathcal{F}^{em} = \mathcal{F}^{am}; \tag{20}$$

where the superscript $(.)^m$ denote a quantity at the mid point t_m (see fig. 1). The discretized inertial forces are

$$\mathcal{F}^{im} = \frac{m\dot{u}^f - m\dot{u}^i}{\Delta t}; \tag{21}$$

and the following velocity-displacement and force-displacement relationships are used

$$\frac{u^f - u^i}{\Delta t} = \frac{\dot{u}^f + \dot{u}^i}{2}; \quad \mathcal{F}^{em} = k\frac{u^f + u^i}{2}. \tag{22}$$

Finally, the discretized applied forces are

$$\mathcal{F}^{am} = \frac{1}{2}\int_{-1}^{1} \mathcal{F}^a(\tau)\, d\tau. \tag{23}$$

Δt indicates the time step size, and τ is a nondimensional time variable such that $\tau = -1.0$ or $+1.0$ at times t_i and t_f, respectively. The properties of this integration scheme can be investigated using the classical techniques for the analysis of linear schemes. The spectral radius of the amplification matrix is always equal to unity, implying unconditional stability. This scheme is identical to the Newmark scheme [2] with $\gamma = 1/2$ and $\beta = 1/4$. It can be readily shown that the discrete equations of motion (20) imply a discrete energy preservation statement $\mathcal{E}^f = \mathcal{E}^i$, where $\mathcal{E} = \mathcal{K} + \mathcal{V}$ is the total mechanical energy.

The same problem can be treated with the time discontinuous Galerkin approximation (13) which writes

$$\int_{t_j}^{t_f} \Big\{ w_1[\dot{u} - \frac{p}{m}] + w_2[\dot{p} + ku - \mathcal{F}^a] \Big\}\, dt + w_1^j\langle u\rangle + w_2^j\langle p\rangle = 0. \tag{24}$$

Using a linear in time approximation for the displacement, momentum, and test functions, the following discrete equations are obtained

$$\mathcal{F}^{im} + \mathcal{F}^{eg} = \mathcal{F}^{ag}; \quad \mathcal{F}^{ih} - \frac{1}{3}[\mathcal{F}^{eg} - f^j] = \mathcal{F}^{ah}. \tag{25}$$

The superscript $(.)^g$ denotes a quantity at the midpoint between t_j and t_f, whereas $(.)^h$ denotes a quantity at the midpoint between t_i and t_j, see fig. 2. The discretized inertial forces are

$$\mathcal{F}^{im} = \frac{m\dot{u}^f - m\dot{u}^i}{\Delta t}; \quad \mathcal{F}^{ih} = \frac{m\dot{u}^j - m\dot{u}^i}{\Delta t}; \tag{26}$$

and the following velocity-displacement and force-displacement relationships are used

$$\frac{u^f - u^i}{\Delta t} = \frac{\dot{u}^f + \dot{u}^j}{2}; \quad 3\frac{u^j - u^i}{\Delta t} = -\frac{\dot{u}^f - \dot{u}^j}{2}; \quad \mathcal{F}^{eg} = k\frac{u^f + u^j}{2}. \tag{27}$$

Finally, the discretized applied forces are

$$\mathcal{F}^{ag} = \frac{1}{2}\int_{-1}^{1} \mathcal{F}^a\, d\tau; \quad \mathcal{F}^{ah} = -\frac{1}{2}\int_{-1}^{1} \mathcal{F}^a\, \tau d\tau. \tag{28}$$

It can be readily shown that the discrete equations of motion (25) imply a discrete energy decay inequality $\mathcal{E}^f \leq \mathcal{E}^i$. This is a direct consequence of (18), since the Hamiltonian is equal to the total energy of the system for this simple problem.

This can be confirmed by a conventional analysis of the scheme based on the characteristics of the amplification matrix. The period elongation is $\Delta T/T = \omega^4\Delta t^4/270 + O(\omega^6\Delta t^6)$,

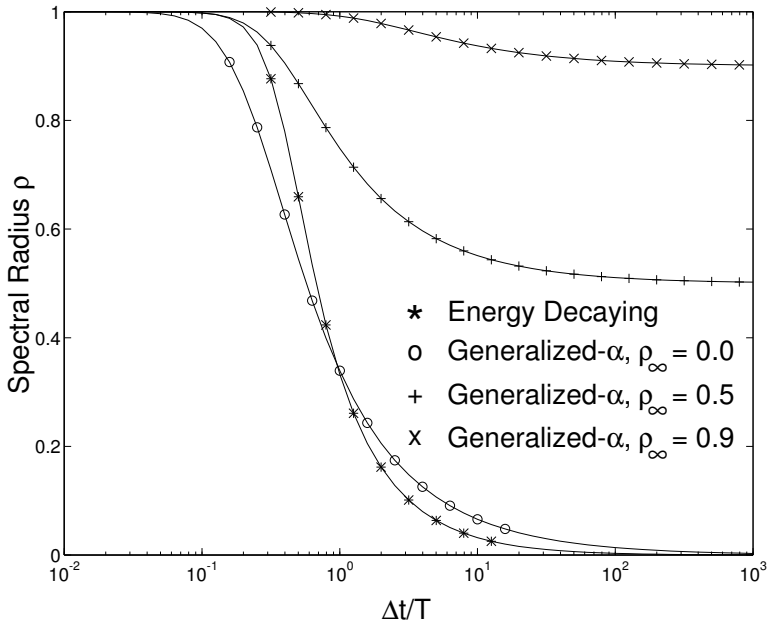

Figure 3: Comparison of spectral radii of various time integration schemes.

while the algorithmic damping is $\zeta = \omega^3 \Delta t^3/72 + O(\omega^5 \Delta t^5)$, where $\omega^2 = k/m$. Hence, the scheme is third-order accurate. The spectral radius, period elongation, and algorithmic damping are shown in figs. 3, 4, and 5, respectively, as functions of $\Delta t/T = \omega \Delta t/(2\pi)$. The results are compared with generalized-α method [5] with three different values of spectral radius at infinity, $\rho_\infty = 0.9$, 0.5, and 0.0. Fig. 4 indicates that the time discontinuous Galerkin scheme has better period elongation characteristics than generalized-α method, while fig. 5 shows that its low frequency numerical dissipation characteristics are similar those of the generalized-α method with $\rho_\infty = 0.5$. Asymptotic annihilation is obtained with the time discontinuous Galerkin scheme. The scheme is unconditionally stable since the spectral radius is always smaller than unity.

2.6 Discussion

Both Galerkin (8) and time discontinuous Galerkin (13) approximations applied to the equations of motion written in the symmetric hyperbolic form (7) have been shown to provide a systematic way of deriving unconditionally stable time integration schemes, provided the Hamiltonian is a positive definite function. The energy decay inequality associated with the time discontinuous Galerkin approximation implies the presence of numerical dissipation in the resulting time integration schemes, whereas such dissipation is ruled out by the strict energy preservation associated with the Galerkin approximation. Since the presence of numerical dissipation is highly desirable, the time discontinuous Galerkin approach appears to be the most promising method.

However, both of these approaches present a major drawback: it is not always possible to recast the equations of motion of general systems into the symmetric hyperbolic

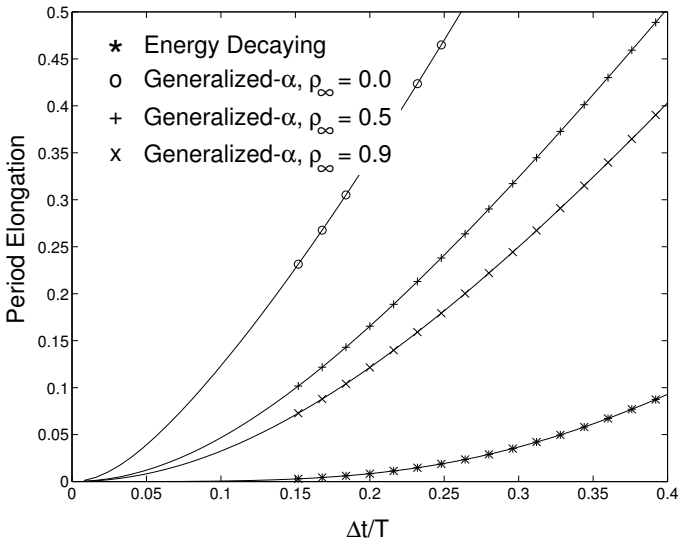

Figure 4: Comparison of period elongation of various time integration schemes.

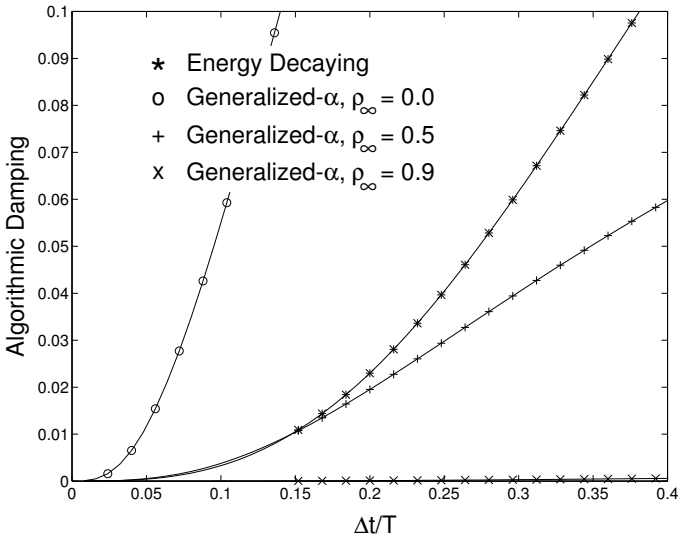

Figure 5: Comparison of algorithmic damping of various time integration schemes.

form. In particular, it does not seem possible to cast the governing equations of constrained multi-body systems in the symmetric hyperbolic form. Furthermore, the time discontinuous Galerkin approach require two level of unknowns (at t_j and t_f). In elasto-dynamics, three fields are required for the symmetric hyperbolic form: displacements, stresses and momenta. Hence, the final discrete equations will involve $6N$ unknowns, resulting in unacceptably high computational cost [13].

3 Practical time integration schemes

In this section, time integration schemes applicable to nonlinear elastic multi-body systems will be developed, without resorting to the symmetric hyperbolic form of the equations of motion. The investigation will focus on dynamical system defined by a kinetic energy $\mathcal{K} = 1/2\ M_{pq}\ v_p\ v_q$ and a strain energy $\mathcal{V} = 1/2\ C_{pq}\ \varepsilon_p\ \varepsilon_q$. The mass matrix M_{pq} and stiffness matrix C_{pq} are symmetric and definite positive; the velocities and strains are given as $v_p = R_{pq}(u_r)\dot{u}_q$, and $\varepsilon_p = \varepsilon_p(u_r)$, respectively. Note that the velocities are assumed to be linear functions of the $\dot{u}_p$, resulting in a kinetic energy that is a quadratic form in $\dot{u}_p$. Under these conditions the total mechanical energy of the system is preserved [22].

The equations of motion of such systems simply write $\mathcal{F}^i_p + \mathcal{F}^e_p = \mathcal{F}^a_p(t)$, where $\mathcal{F}^a_p(t)$ are the time dependent external forces. The inertial and elastic forces, $\mathcal{F}^i_p$ and $\mathcal{F}^e_p$, respectively, are

$$\mathcal{F}^i_p = \frac{d}{dt}(R_{qp}\ p_q) - \dot{u}_r D_{qrp}\ p_q; \quad D_{pqr} = R_{pq,r}, \tag{29}$$

$$\mathcal{F}^e_p = B_{qp}\ f_q; \quad B_{pq} = \varepsilon_{p,q}, \tag{30}$$

where $p_q = M_{qr}\ v_r$ and $f_q = C_{qr}\ \varepsilon_r$. The notation $(.)_{,p}$ indicates a derivative with respect to u_p.

The energy preservation statement can be obtained by evaluating the work done by the inertial, elastic, and applied forces. The work done by the inertial forces is computed first $\mathcal{W}^i = \int_{t_i}^{t_f} \dot{u}_p \mathcal{F}^i_p\ dt = \mathcal{K}^f - \mathcal{K}^i$. Next, the work done by the elastic forces is evaluated $\mathcal{W}^e = \int_{t_i}^{t_f} \dot{u}_p \mathcal{F}^e_p\ dt = \mathcal{V}^f - \mathcal{V}^i$. Finally, the work done by the applied forces is $\mathcal{W}^a = \int_{t_i}^{t_f} \dot{u}_p Q_q\ dt$. Hence, the equations of motion imply the following work balance equation

$$\mathcal{K}^f - \mathcal{K}^i + \mathcal{V}^f - \mathcal{V}^i = \mathcal{W}^a; \quad \Rightarrow \mathcal{E}^f - \mathcal{E}^i = \mathcal{W}^a, \tag{31}$$

where the total mechanical energy $\mathcal{E} = \mathcal{K} + \mathcal{V}$. In the absence of externally applied forces $\mathcal{W}^a = 0$ and the total energy is preserved.

Our goal is to obtain *discretized* equations of motion that will imply an exact energy preservation condition (31), or an energy decay inequality. At first, discretizations of the inertial and elastic forces will proposed, then energy preserving and energy decaying schemes will be derived.

3.1 Discretization of inertial and elastic forces

Consider a time interval t_i t_f, and an approximate solution over this interval, as shown in fig. 1. The following discretizations of the inertial (29) and elastic (30) forces are proposed:

$$\mathcal{F}_p^{im} = \frac{R_{qp}^f\, p_q^f - R_{qp}^i\, p_q^i}{\Delta t} - \frac{u_r^f - u_r^i}{\Delta t} D_{qrp}^m\, \frac{p_q^f + p_q^i}{2}; \tag{32}$$

$$\mathcal{F}_p^{em} = B_{qp}^m\, f_q^m, \tag{33}$$

where the quantities D_{qrp}^m, B_{qp}^m and f_q^m are as yet undetermined. The work done by the discretized inertial forces is $\mathcal{W}^i = (u_p^f - u_p^i)\mathcal{F}_p^{im}$, and regrouping the term yields:

$$\mathcal{W}^i = \frac{u_p^f - u_p^i}{\Delta t}\left\{\left[R_{qp}^f - \frac{u_r^f - u_r^i}{2} D_{qpr}^m\right] p_q^f - \left[R_{qp}^i + \frac{u_r^f - u_r^i}{2} D_{qpr}^m\right] p_q^i\right\}. \tag{34}$$

The following condition is now imposed:

$$v_q^m = \left[R_{qp}^f - \frac{u_r^f - u_r^i}{2} D_{qpr}^m\right] \frac{u_p^f - u_p^i}{\Delta t} = \left[R_{qp}^i + \frac{u_r^f - u_r^i}{2} D_{qpr}^m\right] \frac{u_p^f - u_p^i}{\Delta t}. \tag{35}$$

These relationships now define both D_{qrp}^m and v_p^m. Note that the existence of D_{qrp}^m satisfying (35) is guaranteed by the mean value theorem which states that

$$R_{qp}^f = R_{qp}^i + R_{qp,r}^m (u_r^f - u_r^i); \quad \Rightarrow D_{qpr}^m = R_{qp,r}^m. \tag{36}$$

The work done by the discretized inertial forces now becomes $\mathcal{W}^i = (v_q^f - v_q^i)\; M_{qp}\; v_p^m$.

Next, the work done by the discretized elastic forces is evaluated $\mathcal{W}^e = (u_p^f - u_p^i) B_{qp}^m\; f_q^m$. The following condition is now imposed

$$\varepsilon_q^f - \varepsilon_q^i = B_{qp}^m\; (u_p^f - u_p^i). \tag{37}$$

Here again, the existence of B_{qp}^m satisfying this condition is guaranteed by the mean value theorem which states that

$$\varepsilon_q^f = \varepsilon_q^i + \varepsilon_{q,r}^m (u_r^f - u_r^i); \quad \Rightarrow B_{qr} = \varepsilon_{q,r}^m. \tag{38}$$

The work done by the discretized elastic forces now becomes $\mathcal{W}^e = (\varepsilon_p^f - \varepsilon_p^i)\; f_p^m$.

3.2 Energy Preserving Scheme

The discretized equations of motion for the energy preserving scheme mimic those obtained in section (2.5) for the Galerkin approximation of the linear spring-mass problem (20)

$$\mathcal{F}_p^{im} + \mathcal{F}_p^{em} = \mathcal{F}_p^{am}, \tag{39}$$

where $\mathcal{F}_p^{im}$ and $\mathcal{F}_p^{em}$ are now given by (32) and (33), respectively; and $\mathcal{F}_p^{am} = 1/2 \int_{-1}^{1} \mathcal{F}_p^a(\tau)\, d\tau$, as in eq. (23). The work done by these discretized forces can be evaluated, as was done in

section (3.1). With the help conditions of (35) and (37) equations of motion (39) imply a work balance statement

$$(v_q^f - v_q^i)\ M_{pq}\ v_p^m + (\varepsilon_p^f - \varepsilon_p^i)\ f_p^m = \mathcal{W}^{am}. \tag{40}$$

The following algorithmic velocity-displacement and force-strain relationship are now selected (see eq. (22))

$$v_p^m = \frac{\dot{u}_p^f + \dot{u}_p^i}{2}; \quad f_p^m = C_{pq}\ \frac{\varepsilon_p^f + \varepsilon_p^i}{2}. \tag{41}$$

The work balance equation (40) then becomes

$$\mathcal{K}^f - \mathcal{K}^i + \mathcal{V}^f - \mathcal{V}^i = \mathcal{W}^a; \quad \Rightarrow \mathcal{E}^f - \mathcal{E}^i = \mathcal{W}^a \tag{42}$$

In summary, discretization (39) implies the energy preservation statement (42) provided that relationships (35) and (37) are satisfied, and that the algorithmic velocity-displacement and force-strain relationships (41) are used.

3.3 Energy Decaying Scheme

The discretized equations of motion for the energy decaying scheme mimic those obtained in section (2.5) for the time discontinuous Galerkin approximation of a linear spring-mass system (25)

$$\mathcal{F}_p^{im} + \mathcal{F}_p^{eg} = \mathcal{F}_p^{ag}; \quad \mathcal{F}_p^{ih} - \frac{1}{3}\left[\mathcal{F}_p^{eg} - B_{qp}^h\ f_q^j\right] = \mathcal{F}_p^{ah} \tag{43}$$

where $\mathcal{F}_p^{im}$, and $\mathcal{F}_p^{ih}$ are given by (32) using superscripts $(.)^f$, $(.)^i$ and $(.)^j$, $(.)^i$, respectively; $\mathcal{F}_p^{eg}$ is given by (33) using superscripts $(.)^f$, $(.)^j$; and $\mathcal{F}_p^{ag} = 1/2\ \int_{-1}^{1} \mathcal{F}_p^a\ d\tau$ and $\mathcal{F}_p^{ah} = 1/2\ \int_{-1}^{1} \mathcal{F}_p^a\ \tau d\tau$, as in eq. (28).

The work done by the discretized inertial forces is $\mathcal{W}^i = (u_p^f - u_p^i)\mathcal{F}_p^{im} + 3\langle u_p\rangle \mathcal{F}_p^{ih}$. With the help of condition (35) this becomes

$$\mathcal{W}^i = v_p^m M_{pq}(v_q^f - v_q^i) + 3v_p^h M_{pq}\langle v_q\rangle. \tag{44}$$

The work done by the discretized elastic forces is $\mathcal{W}^e = (u_p^f - u_p^i)\mathcal{F}_p^{eg} - \langle u_p\rangle[\mathcal{F}_p^{eg} - B_{qp}^h\ f_q^j]$. With the help of condition (37) this becomes

$$\mathcal{W}^e = (\varepsilon_p^f - \varepsilon_p^j)\ C_{pq}\ f_q^g + \langle \varepsilon_p\rangle\ C_{pq}\ f_q^j. \tag{45}$$

The following velocity-displacement and force-strain relationship are now selected (see eq. (27))

$$v_p^m = \frac{\dot{u}_p^f + \dot{u}_p^j}{2}; \quad 3v_p^h = -\frac{\dot{u}_p^f - \dot{u}_p^j}{2}; \quad f_p^g = C_{pq}\frac{\varepsilon_p^f + \varepsilon_p^j}{2}. \tag{46}$$

The work balance equation now writes

$$\mathcal{E}^f - \mathcal{E}^j + v_p^j\ M_{pq}\ \langle v_q\rangle + f_p^j\ C_{pq}\ \langle \varepsilon_q\rangle = \mathcal{W}^a, \tag{47}$$

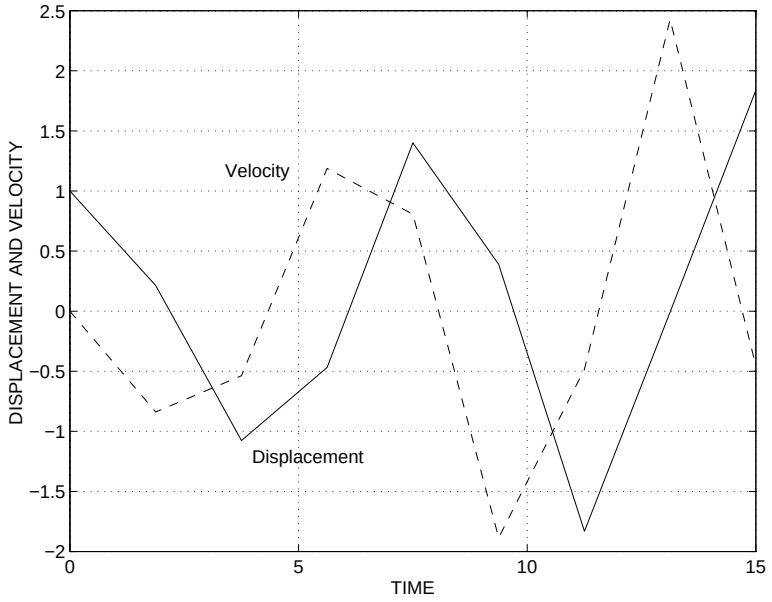

Figure 6: Displacement response for the trapezoidal rule ($u_i = 1.0$).

which mirrors (16). Since the total mechanical energy is a definite positive function of the velocities and strains, the mean value theorem implies

$$\begin{aligned}\mathcal{E}^j &= \mathcal{E}^i + v_p^j\ M_{pq}\ \langle v_q\rangle + f_p^j\ C_{pq}\ \langle \varepsilon_q\rangle - \frac{1}{2}\Big[\mathcal{E}^h_{,v_p v_q}\ \langle v_p\rangle\ \langle v_q\rangle \\ &+\mathcal{E}^h_{,v_p \varepsilon_q}\ \langle v_p\rangle\ \langle \varepsilon_q\rangle + \mathcal{E}^h_{,\varepsilon_p v_q}\ \langle \varepsilon_p\rangle\ \langle v_q\rangle + \mathcal{E}^h_{,\varepsilon_p \varepsilon_q}\ \langle \varepsilon_p\rangle\ \langle \varepsilon_q\rangle\Big] \\ &= \mathcal{E}^i + v_p^j\ M_{pq}\ \langle v_q\rangle + f_p^j\ C_{pq}\ \langle \varepsilon_q\rangle - c^2, \end{aligned} \tag{48}$$

which is equivalent to (17). Combining (47) and (48) then finally yields

$$\mathcal{E}^f = \mathcal{E}^i - c^2 + \mathcal{W}^a; \quad \Rightarrow \mathcal{E}^f \leq \mathcal{E}^i + \mathcal{W}^a. \tag{49}$$

In summary, discretization (43) implies the energy decay statement (49) provided that relationships (35) and (37) are satisfied, and that the algorithmic velocity-displacement and force-strain relationships (46) are used.

3.4 Example: Nonlinear spring-mass system

Consider the nonlinear spring mass oscillator defined by a kinetic energy $\mathcal{K} = 1/2\ m\ \dot{u}^2$, a strain energy $\mathcal{V} = 1/2\ k\ \varepsilon^2$, and a strain $\varepsilon = u^2$. For this example $m = k = 1.0$. It is clear that condition (37) implies $B^m = u^f + u^i$ in this case, and $f^m = k(\varepsilon^f + \varepsilon^i)/2$. The discretized equations of motion are

$$\frac{m\dot{u}^f - m\dot{u}^i}{\Delta t} + 2\ k\left(\frac{u^f + u^i}{2}\right)^3 = 0; \tag{50}$$

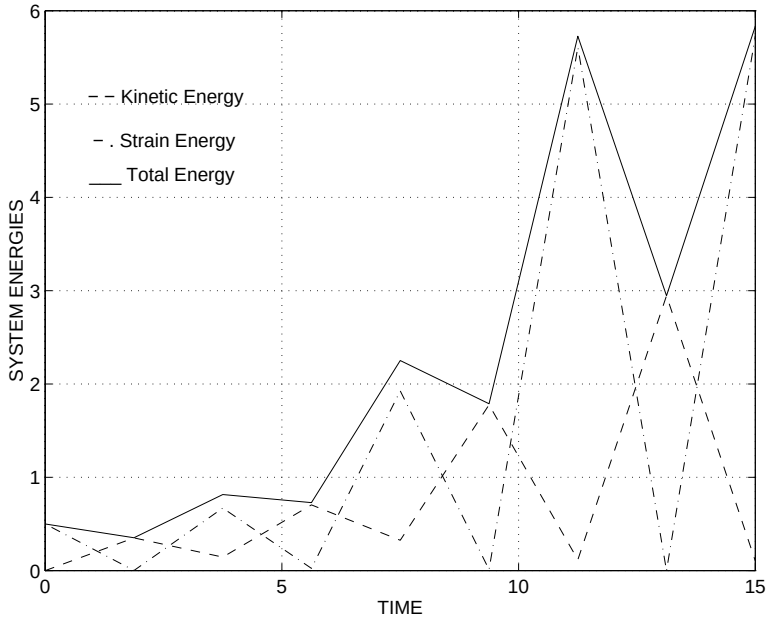

Figure 7: Energy response for the trapezoidal rule ($u_i = 1.0$).

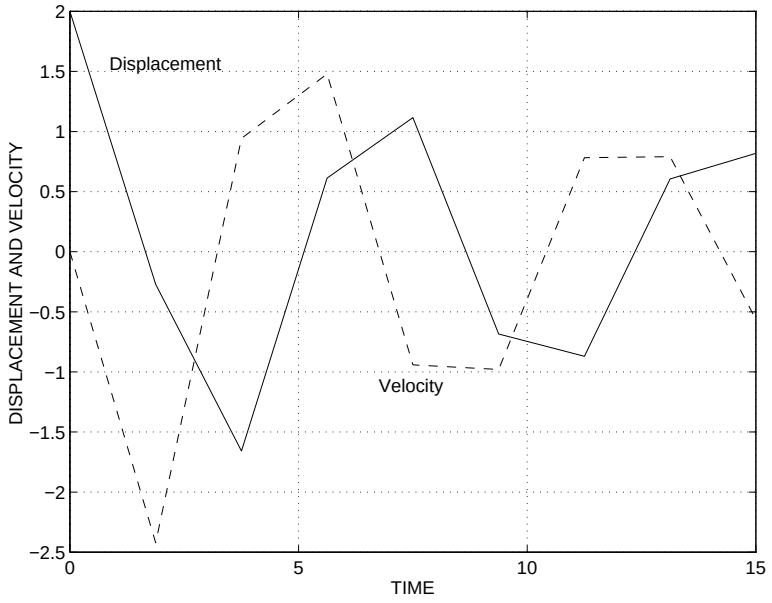

Figure 8: Displacement response for the trapezoidal rule ($u_i = 2.0$).

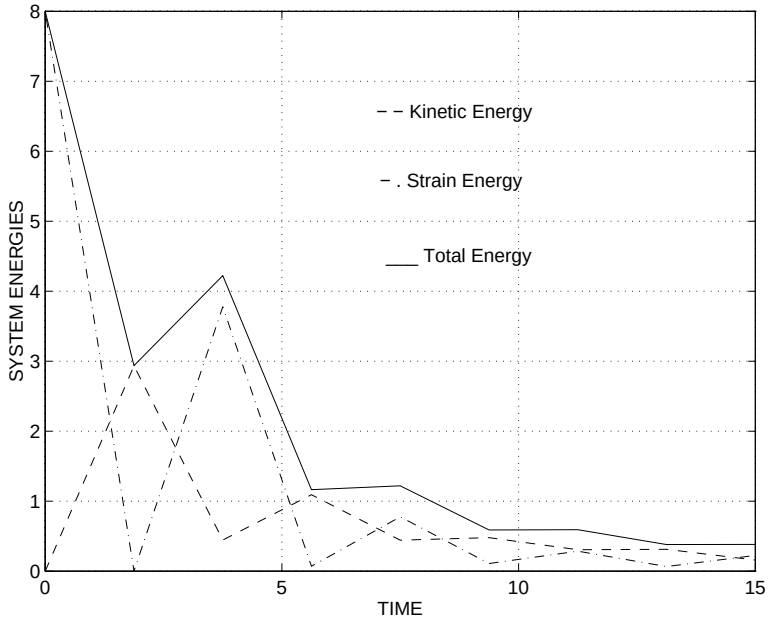

Figure 9: Energy response for the trapezoidal rule ($u_i = =2.0$).

for the trapezoidal rule,

$$\frac{m\dot{u}^f - m\dot{u}^i}{\Delta t} + B^m \; f^m = 0; \tag{51}$$

for the energy decaying scheme, and

$$\frac{m\dot{u}^f - m\dot{u}^i}{\Delta t} + B^g \; f^g = 0, \quad \frac{m\dot{u}^j - m\dot{u}^i}{\Delta t} - \frac{1}{3}\left[B^g \; f^g - B^h \; k \; \varepsilon^j\right] = 0; \tag{52}$$

for the energy decaying scheme.

Though the trapezoidal rule scheme is unconditionally stable for linear system, there is no guarantee of stability when applied to nonlinear systems. Fig. 6 shows the response of the system for initial conditions $u_0 = 1.0$, $\dot{u}_0 = 0.0$. The total energy rapidly increases as shown by fig. 7. For initial conditions $u_0 = 2.0$, $\dot{u}_0 = 0.0$, the corresponding results are shown in figs. 8 and 9, which now show a rapid decrease in energy. The responses predicted by the energy preserving scheme are shown in figs. 10 and 11; as expected, the total energy of the system is exactly preserved. Finally, figs. 12 and 13 show the responses predicted by the energy decaying scheme; the total energy of the system decays, as expected. The results of a convergence study shown in fig. 14 indicate second order accuracy for the trapezoidal rule and the energy preserving scheme, and third order accuracy for the energy decaying scheme.

4 Enforcement of the constraints

4.1 Work done by the forces of constraint

Consider a multi-body system subjected to holonomic constraints $\mathcal{C}_p(u_r) = 0$. If the Lagrange multiplier method is used to enforce these constraints, a constraint potential $\mathcal{V}^c = \lambda_p \mathcal{C}_p$ is

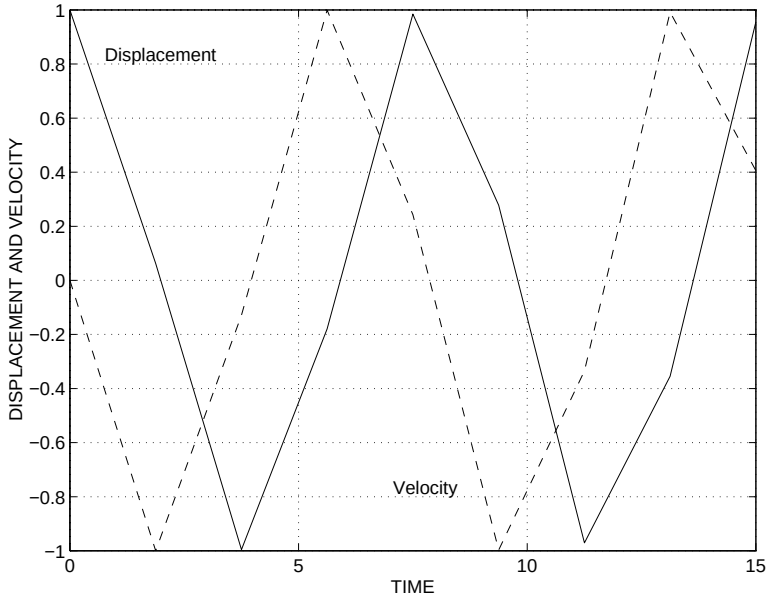

Figure 10: Displacement response for the energy preserving scheme.

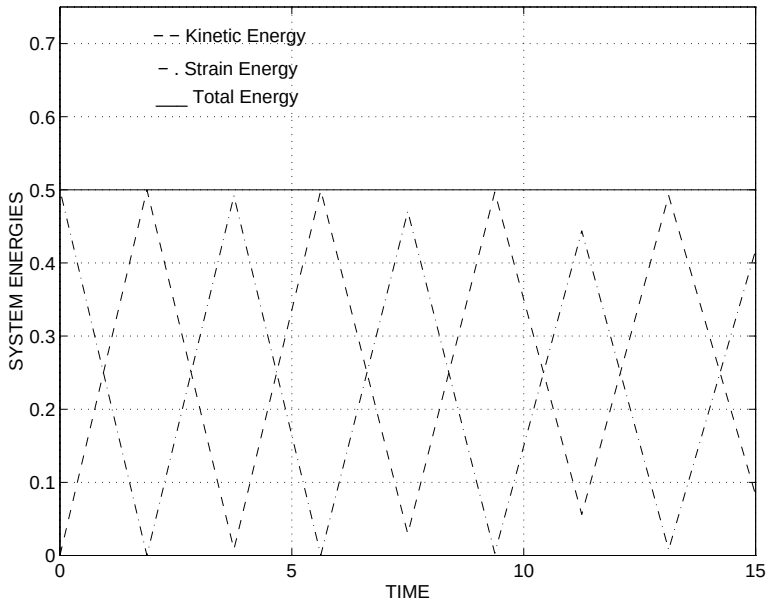

Figure 11: Energy response for the energy preserving scheme.

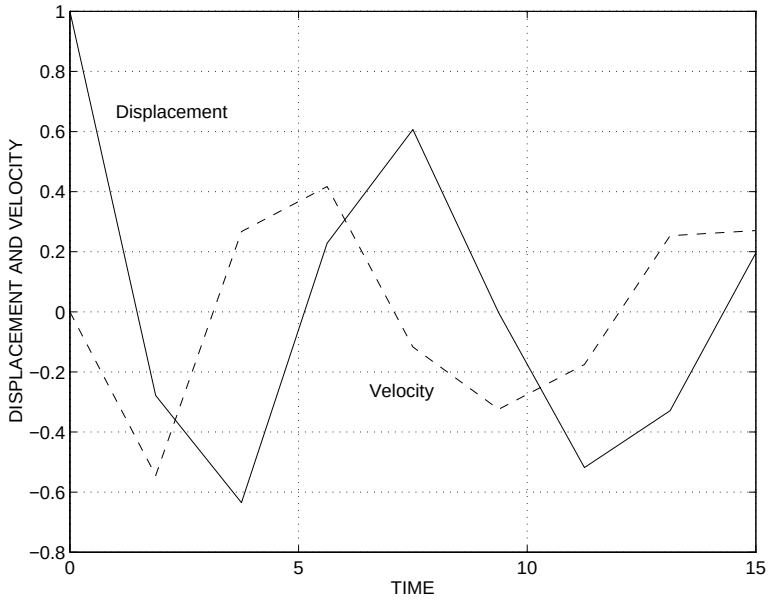

Figure 12: Displacement response for the energy decaying scheme.

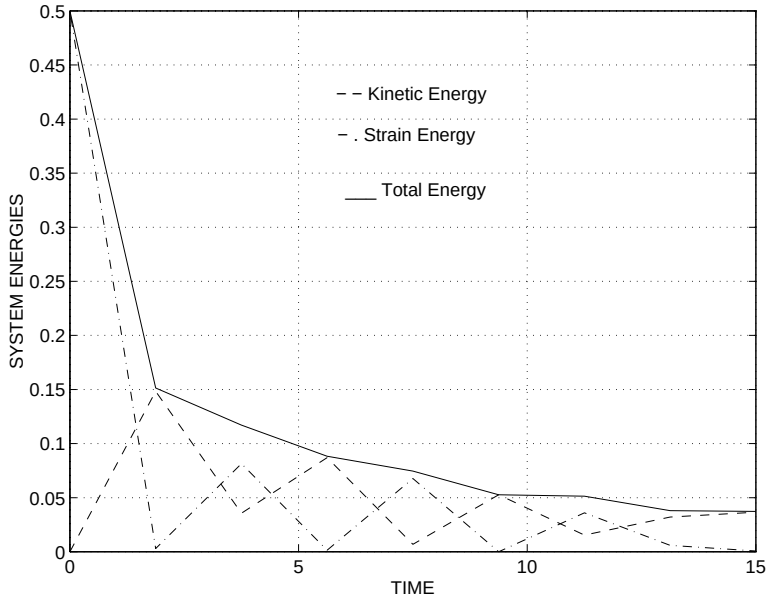

Figure 13: Energy response for the energy decaying scheme.

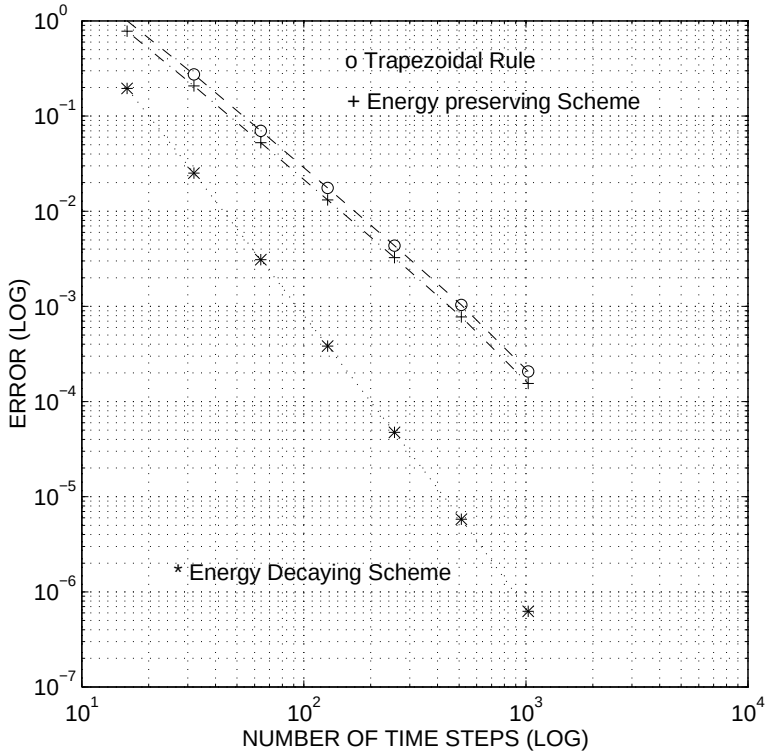

Figure 14: Convergence study.

added to the strain energy of the system, where λ_p are the Lagrange multipliers. The corresponding forces of constraint are

$$\mathcal{F}_p^c = B_{qp}\lambda_q; \quad B_{pq} = \mathcal{C}_{p,q}. \tag{53}$$

The work done by these forces is $\mathcal{W}^c = \int_{t_i}^{t_f} \dot{u}_p \mathcal{F}_p^c \; dt = \int_{t_i}^{t_f} \lambda_p \dot{\mathcal{C}}_p \; dt$. Since $\mathcal{C}_p$ must vanish at all times, $\dot{\mathcal{C}}_p = 0$, and $\mathcal{W}^c = 0$, *i.e.* the work done by the forces of constraint vanishes exactly.

Another method of enforcing constraints is the penalty method. In this approach, a constraint potential $\mathcal{V}^c = \frac{1}{2} P_{pq} \, \mathcal{C}_p \mathcal{C}_q$ is added to the strain energy of the system. $P_{pq} = p \, \delta_{pq}$ is the penalty matrix. There is a close analogy between the constraint potential and the strain energy of an elastic medium: the constraint can be viewed as a strain quantity and the penalty as a stiffness coefficient. As the "stiffness" p increases, the "strains" $\mathcal{C}_p$ become smaller and smaller. At the limit, we let the penalty coefficient increase to infinity so as to drive the constraints to zero, while the product $P_{pq}\mathcal{C}_q/2$ goes to a finite value λ_p. This writes

$$\mathcal{V}^c = \lim_{\substack{p \to \infty \\ \mathcal{C}_p \to 0}} (\frac{1}{2} \, P_{pq} \, \mathcal{C}_q) \, \mathcal{C}_p = \lambda_p \mathcal{C}_p. \tag{54}$$

Hence, the Lagrange multiplier method can be viewed as the limiting case of the penalty method when the penalty coefficient goes to infinity.

4.2 Energy preserving scheme

When the penalty method is used, the forces of constraint can be discretized as if they were elastic forces, see section (3.2). The discretized forces of constraint are $\mathcal{F}_p^{cm} = B_{qp}^m \, f_q^m$, and the following condition is imposed (see eq. (37))

$$\mathcal{C}_q^f - \mathcal{C}_q^i = B_{qp}^m \, (u_p^f - u_p^i), \tag{55}$$

which defines B_{qp}^m. The work done by the forces of constraint is then $\mathcal{W}^c = \mathcal{V}^{cf} - \mathcal{V}^{ci}$. This approach presents two major drawbacks: the constraints are not enforced exactly since a finite value of the penalty coefficient must be used, and as a result, the work done by the forces of constraint does not vanish.

To avoid these problem, the Lagrange multiplier approach will be used. The discretized forces of constraint can be readily obtained through the limiting process mentioned earlier

$$\mathcal{F}_p^{cm} = B_{qp}^m \, \lambda_q^m, \tag{56}$$

and their work then becomes $\mathcal{W}^c = (\mathcal{C}_p^f - \mathcal{C}_p^i) \, \lambda_p^m$. The Lagrange multipliers λ_p^m are now additional unknowns of the problem. The additional equations required to solve the problem are obtained by enforcing the exact vanishing for the work done by the discretized forces of constraint. Since $\lambda_p^m \neq 0$, this implies $\mathcal{C}_p^f - \mathcal{C}_p^i = 0$. In order to avoid the drift phenomenon, it is preferable to enforce the condition $\mathcal{C}_p^f = 0$ at each time step.

In summary, the discretization of the forces of constraint (56) together with relationship (55) and the discrete constraint $\mathcal{C}_p^f = 0$ imply the exact vanishing of the work done by the discretized forces of constraint.

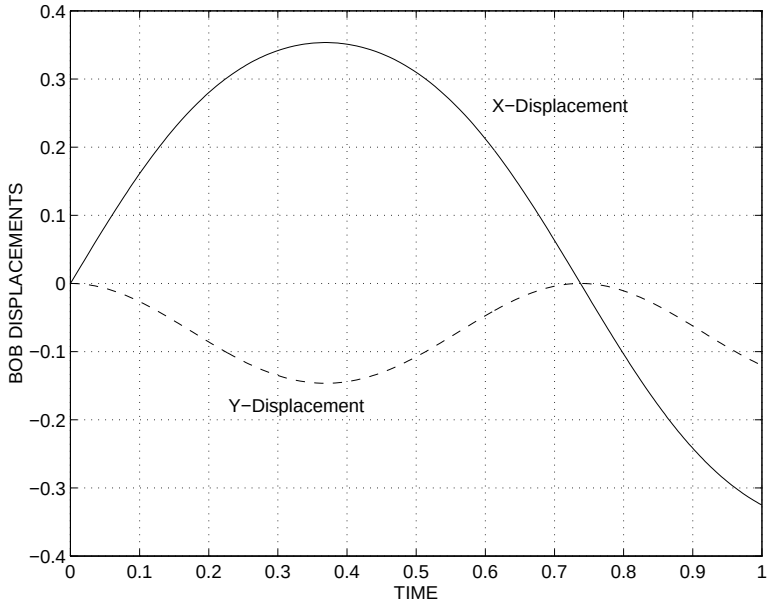

Figure 15: Displacement response for the trapezoidal rule.

4.3 Energy decaying scheme

The Lagrange multiplier method for the energy decaying scheme is also obtained as the limiting case of the penalty approach. The discretized forces of constraint are (see eq. (43))

$$\mathcal{F}_p^{cg} = B_{qp}^g \; \lambda_q^g; \quad \mathcal{F}_p^{ch} = -\frac{1}{3}\left[\mathcal{F}_p^{cg} - B_{qp}^h \; \lambda_q^j\right]. \tag{57}$$

The work done by these forces become $\mathcal{W}^c = (\mathcal{C}_p^f - \mathcal{C}_p^j) \; \lambda_p^g + (\mathcal{C}_p^j - \mathcal{C}_p^i) \; \lambda_p^g$, and vanishes only if $\mathcal{C}_p^f - \mathcal{C}_p^j = 0$ and $\mathcal{C}_p^j - \mathcal{C}_p^i = 0$. Here again it is preferable to enforce $\mathcal{C}_p^f = \mathcal{C}_p^j = 0$ to avoid the drift phenomenon. In summary, the discretization of the forces of constraint (57) together with the discrete constraints $\mathcal{C}_p^f = \mathcal{C}_p^j = 0$ imply the exact vanishing of the work done by the discretized forces of constraint.

4.4 Example: the pendulum problem

Consider the pendulum problem defined by a kinetic energy $\mathcal{K} = 1/2 \; m \; \dot{u}_p \dot{u}_p$, a potential energy $\mathcal{V} = -m \; g \; u_2$, and the constraint $\mathcal{C} = 1/2(u_p u_p - l^2) = 0$, where l is the length of the pendulum. For this example $m = 1.0 \; kg$, $l = 0.5 \; m$; $v_0 = 1.695 \; m/sec$; and $g = 9.81 \; m/sec^2$. It is clear that condition (55) implies $B_p^m = u_p^m$, where $u_p^m = 1/2 \; (u_p^f + u_p^i)$. The governing equations for the trapezoidal rule and energy preserving schemes are

$$\frac{m\dot{u}_p^f - m\dot{u}_p^i}{\Delta t} + B_p^m \; \lambda^m = m g_p. \tag{58}$$

For the trapezoidal rule the constraint condition is $\mathcal{C}^m = 1/2 \; [u_p^m u_p^m - l^2] = 0$, whereas for the energy preserving it is $\mathcal{C}^f = 1/2 \; [u_p^f u_p^f - l^2] = 0$. Finally, the governing equations for the

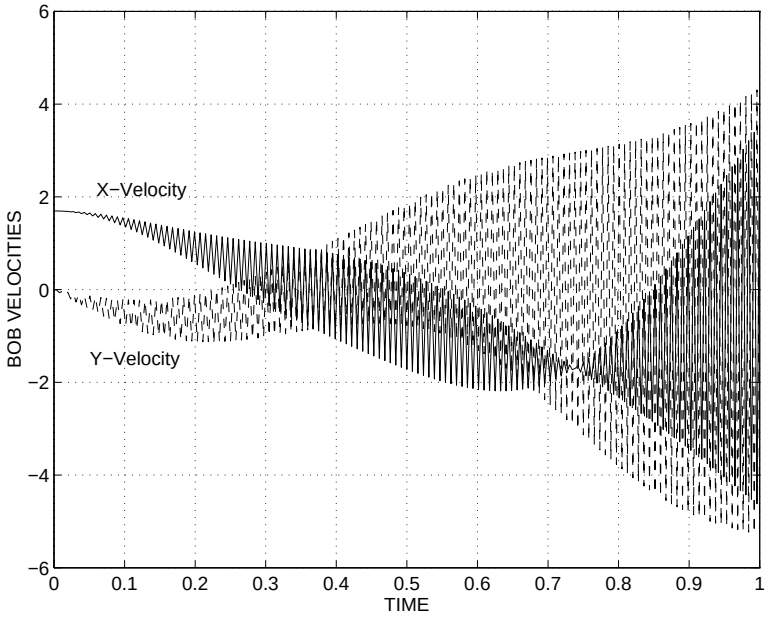

Figure 16: Velocity response for the trapezoidal rule.

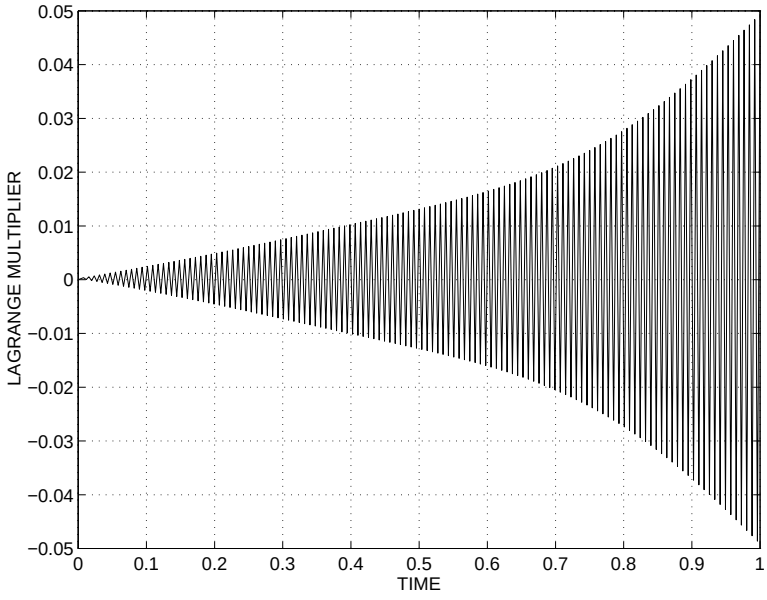

Figure 17: Lagrange multiplier response for the trapezoidal rule.

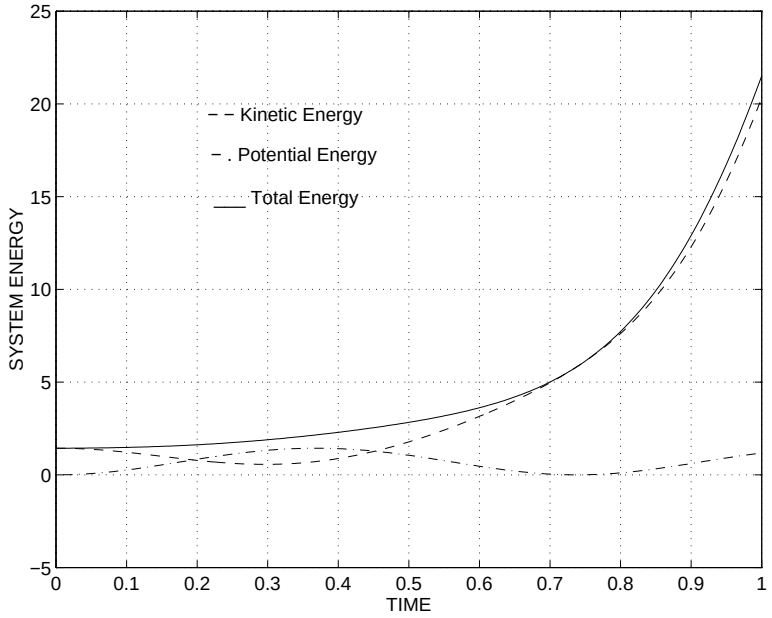

Figure 18: Energy response for the trapezoidal rule.

energy decaying scheme are

$$\frac{m\dot{u}_p^f - m\dot{u}_p^i}{\Delta t} + B_p^g\ \lambda^g = mg_p; \tag{59}$$

$$\frac{m\dot{u}_p^j - m\dot{u}_p^i}{\Delta t} - \frac{1}{3}\left[B_p^g\ \lambda^g - B_p^h\ \lambda^j\right] = 0; \tag{60}$$

subjected to two constraint condition $\mathcal{C}^f = 0$, and $\mathcal{C}^j = 1/2\ [u_p^j u_p^j - l^2] = 0$.

Fig. 15, 16 and 17 show the time history of the pendulum displacements, velocities, and Lagrange multiplier, respectively, for the trapezoidal rule. Though the displacement history is accurately predicted, the velocities and Lagrange multipliers present violent oscillations of a purely numerical origin. The sharp rise in total energy shown in fig. 18 clearly indicates the unstable nature of this scheme. Figs. 19 to 22 show the corresponding results for the energy preserving and decaying schemes which are in very close agreement. All predicted histories are smooth. The total energy is exactly preserved for the energy preserving scheme, and for the energy decaying scheme, the amount of dissipated energy is very small for this simple problem.

5 Kinematic notations and conventions

The kinematic description of bodies and joints in their undeformed and deformed configurations will make use of three orthogonal triads. First, an inertial triad is used as a global reference for the system; it is denoted $\mathcal{S}_I$ with unit vectors $\vec{i}_1$, $\vec{i}_2$, and $\vec{i}_3$. A second triad $\mathcal{S}_0$, with unit vectors $\vec{e}_{01}$, $\vec{e}_{02}$, and $\vec{e}_{03}$ is attached to the body and defines its orientation in the

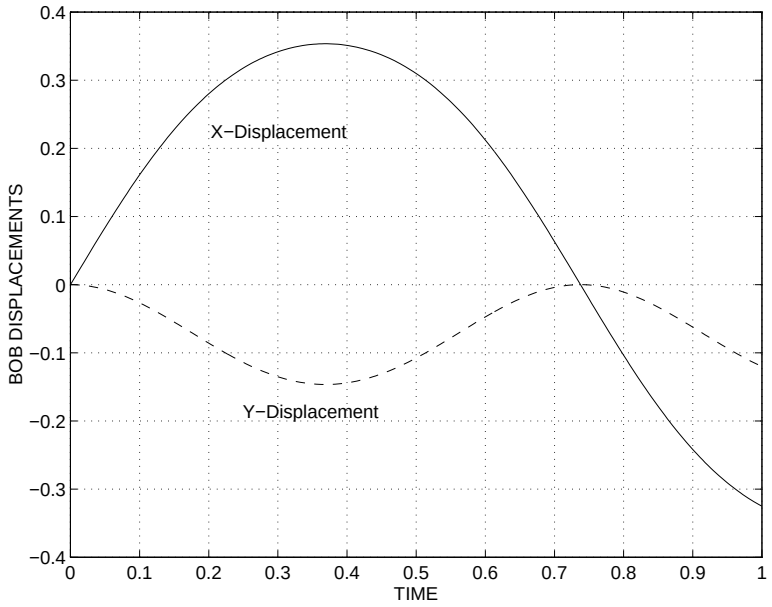

Figure 19: Displacement response for the energy preserving and decaying schemes.

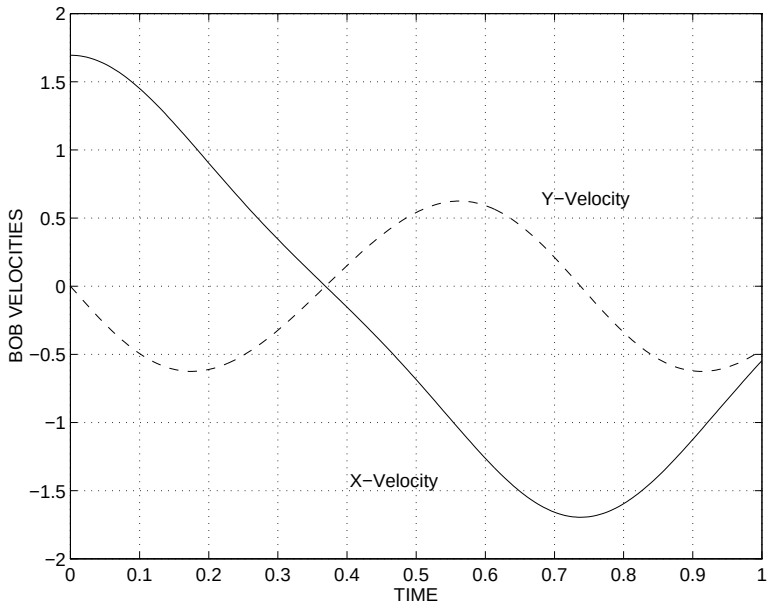

Figure 20: Velocity response for the energy preserving and decaying schemes.

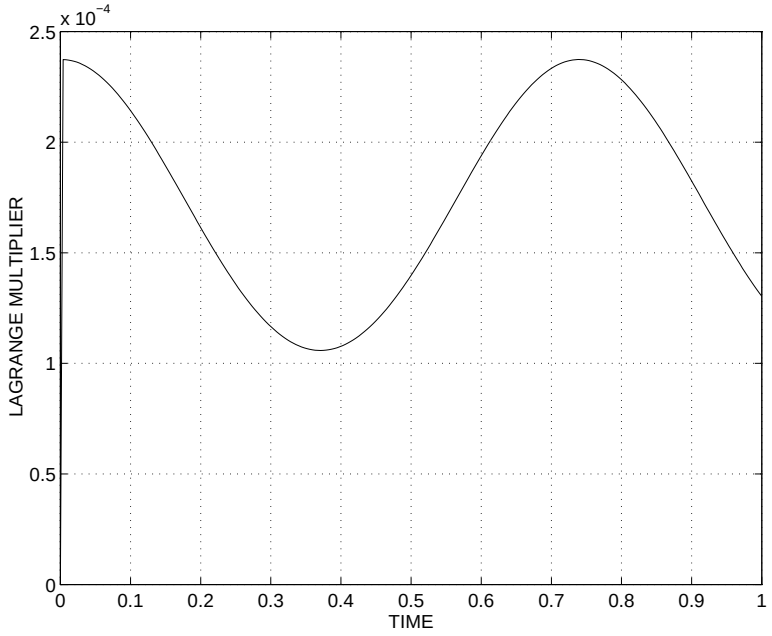

Figure 21: Lagrange multiplier response for the energy preserving and decaying schemes.

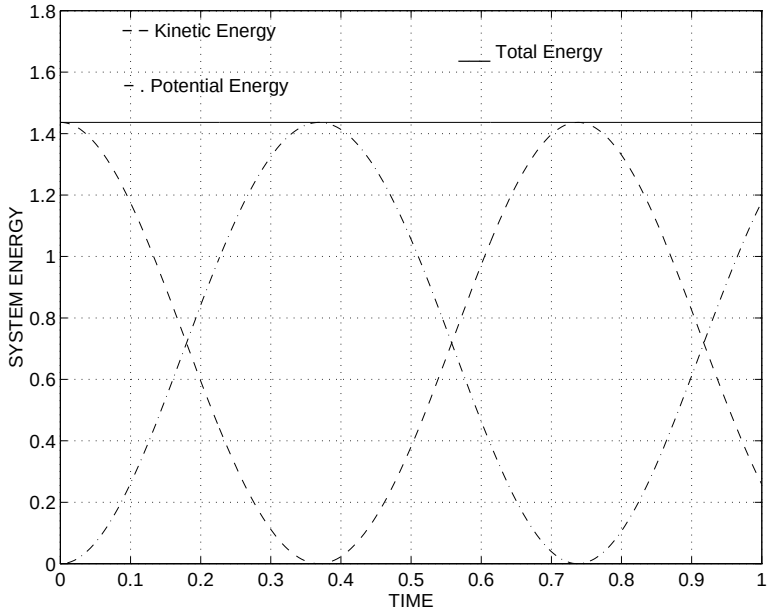

Figure 22: Energy response for the energy preserving and decaying schemes.

reference configuration. Finally, a third triad $\mathcal{S}^*$ with unit vectors $\vec{e}_1$, $\vec{e}_2$, and $\vec{e}_3$ defines the orientation of the body in its deformed configuration.

Let $\vec{u}_0$ and $\vec{u}$ be the displacement vectors from $\mathcal{S}_I$ to $\mathcal{S}_0$, and $\mathcal{S}_0$ to $\mathcal{S}^*$, respectively, and $\mathbf{R}_0$ and $\mathbf{R}$ the rotation tensors from $\mathcal{S}_I$ to $\mathcal{S}_0$, and $\mathcal{S}_0$ to $\mathcal{S}^*$, respectively. In this work, all vector and tensor components are measured in either $\mathcal{S}_I$ or $\mathcal{S}^*$. For instance, the components of vector $\vec{u}$ measured in $\mathcal{S}_I$ and $\mathcal{S}^*$ will be denoted $\underline{u}$ and $\underline{u}^*$, respectively, and clearly

$$\underline{u}^* = R_0^T R^T \ \underline{u}. \tag{61}$$

Similarly, the components of tensor $\mathbf{R}$ measured $\mathcal{S}_I$ and $\mathcal{S}^*$ will be denoted R and R^*, respectively. For brevity sake, a compact notation will be used to deal with the components of the linear and angular vectors simultaneously. For instance,

$$\underline{v} = \begin{bmatrix} \hat{\underline{v}} \\ \check{\underline{v}} \end{bmatrix} \tag{62}$$

defines the six components of the velocity vector consisting of the three components linear and angular velocities denoted $\hat{\underline{v}}$ and $\check{\underline{v}}$, respectively. The following 6×6 operators are introduced

$$\mathcal{R}_0 = \begin{bmatrix} R_0 & 0 \\ 0 & R_0 \end{bmatrix}; \quad \mathcal{R} = \begin{bmatrix} R & 0 \\ 0 & R \end{bmatrix}; \quad \mathcal{U}[.] = \begin{bmatrix} 0 & 0 \\ [.] & 0 \end{bmatrix}. \tag{63}$$

The skew-symmetric matrix formed with the components $\underline{u}$ will be denoted $\widetilde{u}$.

6 Formulation elastic elements

6.1 Formulation of beam elements

Beams can be defined as elastic bodies whose volume is that spanned by a cross-section translating along a smooth reference line. The cross-section lies in the plane defined by vectors $\vec{e}_{02}$, $\vec{e}_{03}$ and $\vec{e}_2$, $\vec{e}_3$ in the undeformed and deformed configurations, respectively, as depicted in fig. 23. The kinetic and strain energies of the beam are

$$\mathcal{K} = \frac{1}{2} \int_0^L \underline{v}^{*T} M^* \underline{v}^* \ dx_1; \quad \mathcal{V} = \frac{1}{2} \int_0^L \underline{e}^{*T} C^* \underline{e}^* \ dx_1, \tag{64}$$

respectively. L is the length of the beam; x_1 the curvilinear coordinate along the reference line; M^* and C^* the components of the sectional inertial and stiffness tensor, respectively; and $\underline{v}^*$, and $\underline{e}^*$ the components of the sectional velocity and strain vectors, respectively. The 6×6 inertial matrix M^* is fully populated, allowing the modeling of rotary inertia effects and the offset of the sectional mass center with respect to the reference line. Similarly, the 6×6 stiffness matrix C^* is fully populated, allowing the modeling of shearing deformation effect, the offset of tension center and shear center with respect to the reference line, and all elastic couplings that might arise from the use of tailored composite materials. The velocity-displacement and strain-displacement relationships are

$$\underline{v} = \begin{bmatrix} \hat{\underline{v}} \\ \check{\underline{v}} \end{bmatrix} = \begin{bmatrix} \dot{\underline{u}} \\ \check{\underline{v}} \end{bmatrix}; \quad \underline{e} = \begin{bmatrix} \hat{\underline{e}} \\ \check{\underline{e}} \end{bmatrix} = \begin{bmatrix} (\underline{u}_0' + \underline{u}') - RR_0 \ \underline{\imath}_1 \\ \check{\underline{e}} \end{bmatrix}, \tag{65}$$

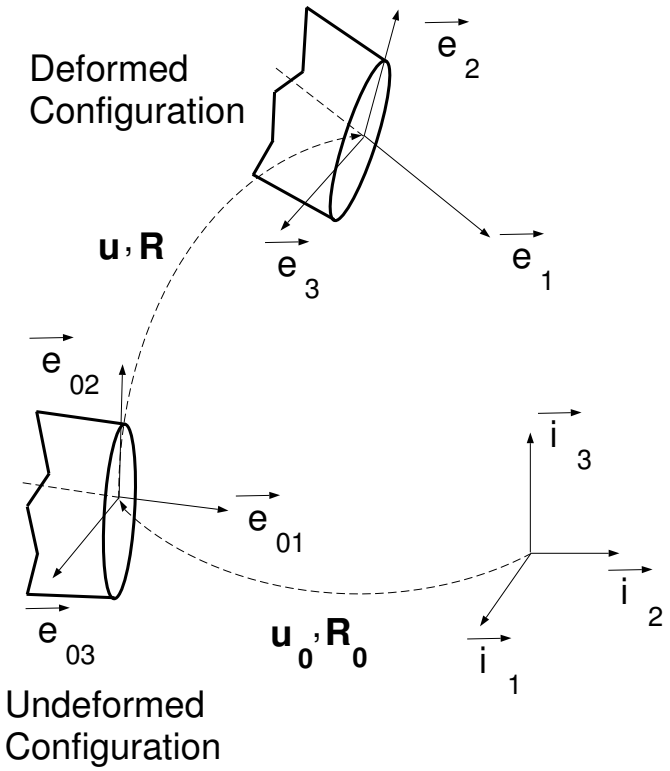

Figure 23: Beam in the undeformed and deformed configurations.

where $(.)^{\cdot}$ and $(.)'$ denote derivatives with respect to time and x_1, respectively; $\underline{\check{v}}$ are the components of the sectional angular velocity vector, with $\widetilde{\check{v}} = \dot{R}\, R^T$; and $\underline{\check{e}}$ the components of the sectional elastic curvature vector, with $\widetilde{\check{e}} = R'R^T$. These relationships are geometrically exact, *i.e.* are valid for arbitrarily large displacements and rotations, although the strains are assumed to remain small. Virtual variations in sectional velocities and strains are

$$\delta \underline{v}^{*T} = \left(\underline{\dot{\delta d}}^T - \underline{\delta d}^T \, \mathcal{U}[\widetilde{\dot{u}}] \right) \mathcal{R}\mathcal{R}_0; \tag{66}$$

$$\delta \underline{e}^{*T} = \left(\underline{\delta d}'^T - \underline{\delta d}^T \, \mathcal{U}[\widetilde{u}'_0 + \widetilde{u}'] \right) \mathcal{R}\mathcal{R}_0, \tag{67}$$

where $\underline{\delta d}^T = (\delta \underline{u}^T, \ \underline{\delta \psi}^T)$ are the virtual displacements and rotations. The virtual rotations are defined as $\widetilde{\delta\psi} = \delta R \; R^T$.

The equations of motion of the beam will be derived from Hamilton's principle

$$\int_{t_i}^{t_f} \int_0^L \left(\delta \underline{v}^{*T} M^* \underline{v}^* - \delta \underline{e}^{*T} C^* \underline{e}^{*T} + \delta \mathcal{W}^a \right) dx_1 \; dt = 0, \tag{68}$$

where $\delta \mathcal{W}^a$ is the virtual work done by the externally applied forces. The equations of motion of the beam are found by introducing eqs. (66) and (67), and using the strain and velocity expressions, eqs. (65), to find

$$\left(\mathcal{R}\mathcal{R}_0 \; \underline{p}^* \right)^{\cdot} + \mathcal{U}[\dot{\widetilde{u}}] \; \mathcal{R}\mathcal{R}_0 \; \underline{p}^* - \left(\mathcal{R}\mathcal{R}_0 \; \underline{f}^* \right)' - \mathcal{U}[\widetilde{u}'_0 + \widetilde{u}'] \; \mathcal{R}\mathcal{R}_0 \; \underline{f}^* = \underline{q}; \tag{69}$$

where the sectional momenta and elastic forces are defined as $\underline{p}^* = M^* \; \underline{v}^*$ and $\underline{f}^* = C^* \; \underline{e}^*$, respectively; and $\underline{q}$ are the external forces.

An energy preserving discretization of these equations of motion is now sought. The inertial and elastic forces are discretized according to eqs. (32) and (33), to yield the following discretized equations of motion

$$\begin{aligned} &\frac{\mathcal{R}_f\mathcal{R}_0 \; \underline{p}^*_f - \mathcal{R}_i\mathcal{R}_0 \; \underline{p}^*_i}{\Delta t} + \mathcal{U}[\frac{\widetilde{u}_f - \widetilde{u}_i}{\Delta t}] \; \mathcal{R}_a\mathcal{R}_0 \; \frac{\underline{p}^*_f + \underline{p}^*_i}{2} \\ &-(\mathcal{R}_b\mathcal{R}_0 \; \underline{f}^*_m)' - \mathcal{U}[\widetilde{u}'_0 + \widetilde{u}'_m] \; \mathcal{R}_b\mathcal{R}_0 \; \underline{f}^*_m = \underline{q}_m, \end{aligned} \tag{70}$$

where the elastic forces $\underline{f}^*_m$ are as yet undetermined; $\underline{u}_m = (\underline{u}_f + \underline{u}_i)/2$; and the rotation operators are defined in Appendix B which also discusses the discretization of finite rotations.

The work done by the discretized inertial forces can be computed by premultiplying these forces by the incremental displacements and rotations, then integrating over the span of the beam to find

$$\begin{aligned} \mathcal{W}^i = \int_0^L &\begin{bmatrix} \underline{u}_f - \underline{u}_i \\ \underline{r} \end{bmatrix}^T \left[\frac{\mathcal{R}_f\mathcal{R}_0 \; \underline{p}^*_f - \mathcal{R}_i\mathcal{R}_0 \; \underline{p}^*_i}{\Delta t} \right. \\ &\left. + \mathcal{U}[\frac{\widetilde{u_f} - \widetilde{u}_i}{\Delta t}] \; \mathcal{R}_a\mathcal{R}_0 \; \frac{\underline{p}^*_f + \underline{p}^*_i}{2} \right] \; dx_1, \end{aligned} \tag{71}$$

where $\underline{r}$ are the components of the Rodrigues parameters used to measure the incremental rotations, see Appendix B. Regrouping terms, this work becomes

$$\begin{aligned} \mathcal{W}^i = \int_0^L &\frac{\underline{u}^T_f - \underline{u}^T_i}{\Delta t} \; R_m R_0 \left[(G^* - \frac{\widetilde{r}^*}{2} \; \frac{G^* + G^{*T}}{2}) \; \underline{\hat{p}}^*_f \right. \\ &\left. -(G^{*T} + \frac{\widetilde{r}^*}{2} \; \frac{G^* + G^{*T}}{2}) \; \underline{\hat{p}}^*_i \right] + \frac{\underline{r}^T}{\Delta t} \; R_m R_0 \; (G^* \; \underline{\check{p}}^*_f - G^{*T} \; \underline{\check{p}}^*_i). \end{aligned} \tag{72}$$

This result mirrors eq. (34). With the help of eqs. (A4) and (A5), the mid-point velocity $\underline{v}_m^*$ defined in eq. (35) becomes

$$\underline{v}_m^* = \begin{bmatrix} R_0^T R_a^T \ \dfrac{\underline{u}_f - \underline{u}_i}{\Delta t} \\ R_0^T R_m^T \ \dfrac{\underline{r}}{\Delta t} \end{bmatrix}, \tag{73}$$

and the work done by the discretized inertial forces reduces to

$$\mathcal{W}^i = \underline{v}_m^{*T} \ M^* \ (\underline{v}_f^* - \underline{v}_i^*). \tag{74}$$

We now turn to the work done by the discretized elastic forces which can be computed by premultiplying these forces by the incremental displacements and rotations, integrating over the span of the beam, then integrating by parts to find

$$\mathcal{W}^e = \int_0^L \left\{ \begin{bmatrix} \underline{u}_f' - \underline{u}_i' \\ \underline{r}' \end{bmatrix}^T + \begin{bmatrix} \underline{u}_f - \underline{u}_i \\ \underline{r} \end{bmatrix}^T \ \mathcal{U} \ [\widetilde{u}_0' + \widetilde{u}_m'] \right\} \ \mathcal{R}_b \ \underline{f}_m^* \ dx_1. \tag{75}$$

Regrouping terms, this work becomes

$$\begin{aligned} \mathcal{W}^e = \int_0^L \Bigg\{ & \underline{\hat{f}}_m^{*T} \ \frac{G^* + G^{*T}}{2} \ \Big[(I - \frac{\widetilde{r^*}}{2}) \ R_0^T R_m^T \ (\underline{u}_0' + \underline{u}_f') \\ & - (I + \frac{\widetilde{r^*}}{2}) \ R_0^T R_m^T \ (\underline{u}_0' + \underline{u}_i') \Big] + \underline{\check{f}}_m^{*T} \ R_0^T R_m^T G H^T \ \underline{r}' \Bigg\} \ dx_1. \end{aligned} \tag{76}$$

With the help of eq. (A6), this reduces to

$$\mathcal{W}^e = \int_0^L \left[\underline{\hat{f}}_m^{*T} (\underline{\hat{e}}_f^* - \underline{\hat{e}}_i^*) + \underline{\check{f}}_m^{*T} (\underline{\check{e}}_f^* - \underline{\check{e}}_i^*) \right] \ dx_1. \tag{77}$$

Combining eqs. (74) and (77) it is now clear that discretization (70) implies the following energy balance equation

$$\int_0^L \left[\underline{v}_m^{*T} \ M^* \ (\underline{v}_f^* - \underline{v}_i^*) + \underline{f}_m^{*T} \ (\underline{e}_f^* - \underline{e}_i^*) \right] dx_1 = \Delta \mathcal{W}_m^a, \tag{78}$$

which mirrors eq. (40). Finally, the following velocity-displacement and force-displacement relationships are selected (see eq. (41)

$$\underline{v}_m^* = \frac{\underline{v}_f^* + \underline{v}_i^*}{2}; \quad \underline{f}_m^* = C^* \ \frac{\underline{e}_f^* + \underline{e}_i^*}{2}. \tag{79}$$

The energy balance equation then implies $\mathcal{E}_f - \mathcal{E}_i = \Delta \mathcal{W}_m^a$, the discrete energy preservation condition. In summary, the energy preserving formulation for beams consists of the discretized equations of motion (70) together with relationships (79). This energy preserving formulation can be readily extended to an energy decaying formulation by following the steps outlined in section 3.3.

6.2 Formulation of flexible joint elements

Consider two bodies denoted with superscripts $(.)^k$ and $(.)^l$, respectively, linked together by linear and torsional springs at a point. In the reference configuration, the flexible joint is defined by two coincident triads $\mathcal{S}_0^k = \mathcal{S}_0^l = \mathcal{S}_0$. In the deformed configuration, the two triads undergo relative displacements and rotations, inducing deformations $\underline{s}$ in the flexible joint. These deformations are selected as the relative displacements and rotations of the two bodies

$$\hat{\underline{s}}^* = R_0^T R^{kT}\ \underline{u}; \quad \check{\underline{s}}^* = \frac{1}{2}\begin{bmatrix} g_{32} - g_{23} \\ g_{13} - g_{31} \\ g_{21} - g_{12} \end{bmatrix} = \frac{1}{2}\begin{bmatrix} R^*_{32} - R^*_{23} \\ R^*_{13} - R^*_{31} \\ R^*_{21} - R^*_{12} \end{bmatrix} = \underline{n}^*\ \sin\phi, \tag{80}$$

where $\underline{u} = \underline{u}^k - \underline{u}^l$ is the relative displacement between the bodies; R^*_{ij} the components of the relative rotation tensor $R^* = R_0^T R^{kT} R^l R_0$; ϕ the magnitude of this relative rotation; $\underline{n}^*$ the unit vector about which it takes place; and

$$g_{\alpha\beta} = \underline{e}^{kT}_\alpha\ \underline{e}^l_\beta. \tag{81}$$

The strain energy in the flexible joint now writes

$$\mathcal{V} = \frac{1}{2}\ \underline{s}^{*T}\ C^*\ \underline{s}^*, \tag{82}$$

where C^* are the components of the flexible joint stiffness tensor. This 6×6 stiffness matrix is fully populated allowing the modeling of the various linear and torsional stiffnesses, as well as potential elastic couplings. The elastic forces $\underline{\mathcal{F}}^e$ in the flexible joint are readily found from variations of the strain energy

$$\delta\mathcal{V} = \begin{bmatrix} \delta\underline{u}^k \\ \delta\underline{\psi}^k \\ \delta\underline{u}^l \\ \delta\underline{\psi}^l \end{bmatrix}^T \cdot \begin{bmatrix} - & R^k R_0\ \hat{\underline{f}}^* \\ & S\ \check{\underline{f}}^* - \widetilde{u}\ R^k R_0\ \hat{\underline{f}}^* \\ & R^k R_0\ \hat{\underline{f}}^* \\ - & S\ \check{\underline{f}}^* \end{bmatrix} = \begin{bmatrix} \delta\underline{u}^k \\ \delta\underline{\psi}^k \\ \delta\underline{u}^l \\ \delta\underline{\psi}^l \end{bmatrix}^T \cdot \underline{\mathcal{F}}^e, \tag{83}$$

where $\underline{f}^* = C^* \underline{s}^*$. The operator S is defined as

$$S = \frac{1}{2}\left[\underline{h}_{32} - \underline{h}_{23}, \quad \underline{h}_{13} - \underline{h}_{31}, \quad \underline{h}_{21} - \underline{h}_{12}\right], \tag{84}$$

where

$$\underline{h}_{\alpha\beta} = \widetilde{e}^k_\alpha\ \underline{e}^l_\beta. \tag{85}$$

An energy preserving discretization is now sought and these elastic forces are discretized according to eq. (33)

$$\underline{\mathcal{F}}^e_m = \begin{bmatrix} - & R^k_a R_0\ \hat{\underline{f}}^*_m \\ & S_m\ \check{\underline{f}}^*_m - \widetilde{u}_m\ R^k_a R_0\ \hat{\underline{f}}^*_m \\ & R^k_a R_0\ \hat{\underline{f}}^*_m \\ - & S_m\ \check{\underline{f}}^*_m \end{bmatrix}, \tag{86}$$

where the rotation operators are defined in Appendix B which also describes the discretization of the finite rotations;

$$S_m = \frac{1}{2}\left[\underline{h}_{32m} - \underline{h}_{23m}, \quad \underline{h}_{13m} - \underline{h}_{31m}, \quad \underline{h}_{21m} - \underline{h}_{12m}\right]; \tag{87}$$

and

$$\underline{e}_{\alpha m} = \frac{\underline{e}_{\alpha f} + \underline{e}_{\alpha i}}{2}; \quad \underline{h}_{\alpha\beta m} = \widetilde{e}^{k}_{\alpha m}\ \underline{e}^{l}_{\beta m}. \tag{88}$$

The work done by these discretized elastic forces writes

$$\mathcal{W}^e = \underline{\hat{f}}^{*T}_{m}\ R^T_0 R^{kT}_a \left[(\underline{u}_f - \underline{u}_i) + \widetilde{u}_m\ \underline{r}^k\right] + \underline{\check{f}}^{*T}_{m}\ S^T_m\ (\underline{r}^k - \underline{r}^l). \tag{89}$$

Regrouping terms and using eqs. (A5) and (A6) then yields

$$\mathcal{W}^e = \underline{\hat{f}}^{*T}_{m}\ (\underline{\hat{s}}^*_f - \underline{\hat{s}}^*_i) + \underline{\check{f}}^{*T}_{m}\ (\underline{\check{s}}^*_f - \underline{\check{s}}^*_i) = \underline{f}^{*T}_{m}\ (\underline{s}^*_f - \underline{s}^*_i). \tag{90}$$

Finally, the following force-displacement relationship

$$\underline{f}^*_m = C^*(\underline{s}^*_f + \underline{s}^*_i)/2 \tag{91}$$

is selected (see eq. (41)) and the work done by the discretized elastic forces become $\mathcal{W}^e = \mathcal{V}_f - \mathcal{V}_i$. In summary, the energy preserving formulation for flexible joints consists of the elastic force discretization (86) together with the constitutive laws (91). This energy preserving formulation can be readily extended to an energy decaying formulation by following the steps outlined in section 3.3.

7 Formulation of constraint elements

7.1 Formulation of universal joint elements

Consider two bodies denoted with superscripts $(.)^k$ and $(.)^l$, respectively, linked together by a universal joint, as depicted in fig. 24. In the undeformed configuration, the universal joint is defined by two triads $\mathcal{S}^k_0$ and $\mathcal{S}^l_0$ with a common origin, and $\vec{e}^{\,k}_{03}$ is orthogonal to $\vec{e}^{\,l}_{03}$. The kinematic constraint associated with a universal joint implies the orthogonality of the corresponding vectors in the deformed configuration

$$\mathcal{C} = \underline{e}^{kT}_{\alpha}\ \underline{e}^{l}_{\beta} = g_{\alpha\beta} = 0, \tag{92}$$

where $\alpha = \beta = 3$. Of course, in the deformed configuration, the origin of the triads is still coincident; this constraint is readily enforced within the framework of finite element formulations by Boolean identification of the corresponding degrees of freedom. As discussed in section 4, holonomic constraints are enforced by the addition of a constraint potential $\lambda\,\mathcal{C}$, where λ is the Lagrange multiplier. The forces of constraint $\underline{\mathcal{F}}^c$ corresponding to eq. (92) are readily obtained as

$$\delta\mathcal{C}\cdot\lambda = \begin{bmatrix} \underline{\delta\psi^k} \\ \underline{\delta\psi^l} \end{bmatrix}^T \cdot \begin{bmatrix} \lambda\ \underline{h}_{\alpha\beta} \\ -\ \lambda\ \underline{h}_{\alpha\beta} \end{bmatrix} = \begin{bmatrix} \underline{\delta\psi^k} \\ \underline{\delta\psi^l} \end{bmatrix}^T \cdot \underline{\mathcal{F}}^c. \tag{93}$$

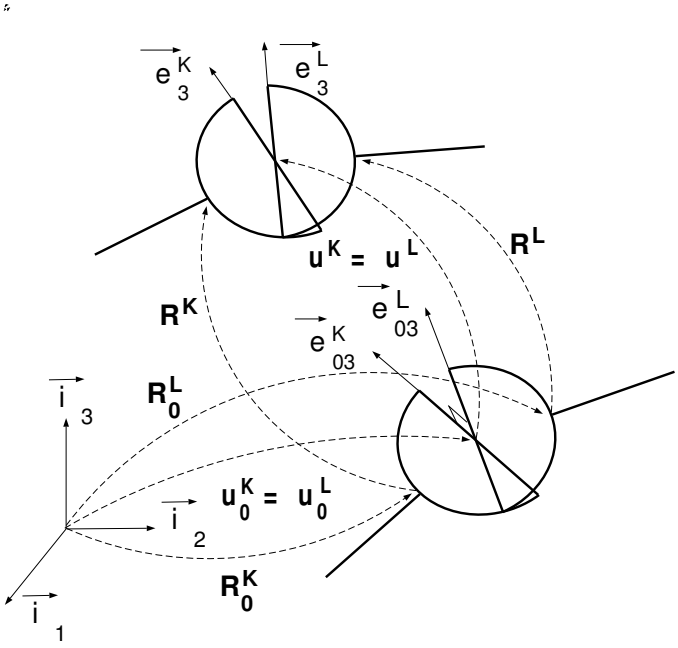

Figure 24: Universal joint in the undeformed and deformed configurations.

To obtain unconditionally stable schemes for constrained systems, these forces of constraint must be discretized so that the work they perform vanishes exactly. The following discretization is proposed

$$\underline{\mathcal{F}}^c_m = \begin{bmatrix} & s\lambda_m & \underline{h}_{\alpha\beta m} \\ - & s\lambda_m & \underline{h}_{\alpha\beta m} \end{bmatrix}, \tag{94}$$

where s is a scaling factor for the Lagrange multipliers, and λ_m the unknown mid-point value of this multiplier. The work done by these constraint forces is computed as follows

$$\begin{aligned} \Delta\mathcal{W}^c &= s\lambda_m(\underline{r}^{kT} - \underline{r}^{lT})\ \underline{h}_{\alpha\beta m} = s\lambda_m\ \underline{i}^T_\alpha\ R^T_0 R^{kT}_m \left[\frac{G^k + G^{kT}}{2}\ \widetilde{r^k}^T \right. \\ &\left. \frac{G^l + G^{lT}}{2} + \frac{G^l + G^{lT}}{2}\ \widetilde{r^l}^T\ \frac{G^k + G^{kT}}{2}\right]\ R^l_m R^T_0\ \underline{i}_\beta \\ &= s\lambda_m\ (\mathcal{C}_f - \mathcal{C}_i), \end{aligned} \tag{95}$$

where the last equality was obtained with the help of eq. (A5). It is now clear that the work done by the discretized constraint forces vanishes if $\mathcal{C}_f - \mathcal{C}_i = 0$. In order to avoid the drift phenomenon, it is preferable to enforce the condition $\mathcal{C}_f = 0$ at each time step. In summary, discretization (94) together with the constraint $\mathcal{C}_f = 0$ leads to the vanishing of the work done by the forces of constraint. This energy preserving formulation can be readily extended to an energy decaying formulation by following the steps outlined in section 4.3.

7.2 Formulation of revolute joint elements

Consider two bodies denoted with superscripts $(.)^k$ and $(.)^l$, respectively, linked together by a revolute joint, as depicted in fig. 25. In the undeformed configuration, the revolute

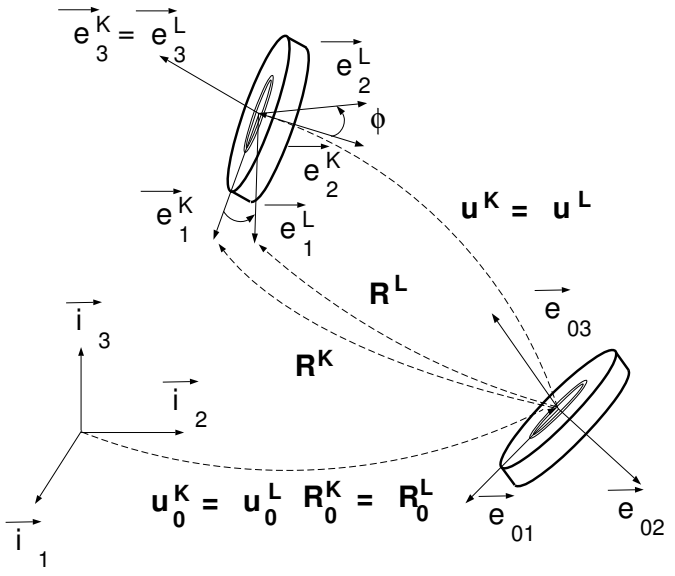

Figure 25: Revolute joint in the undeformed and deformed configurations.

joint is defined by coincident triads $\mathcal{S}_0^k = \mathcal{S}_0^l$. In the deformed configuration, no relative displacements are allowed and the corresponding triads are allowed to rotate with respect to each other in such a way that $\vec{e}_3{}^k = \vec{e}_3{}^l$. This condition implies the orthogonality of $\vec{e}_3{}^k$ to both $\vec{e}_1{}^l$ and $\vec{e}_2{}^l$. These two kinematic constraints are both given by eq. (92) with $\alpha = 3,\ \beta = 1$, and $\alpha = 3,\ \beta = 2$, respectively, and are enforced in the manner described in the previous section. The relative rotation ϕ between the two bodies is defined by adding to the revolute joint formulation a third constraint

$$\mathcal{C} = g_{\alpha\alpha} \sin\phi + g_{\alpha\beta} \cos\phi = 0, \tag{96}$$

where $\alpha = 1$ and $\beta = 2$. Here again, this constraint is enforced via the Lagrange multiplier technique. The corresponding forces of constraint $\underline{\mathcal{F}}^c$ are readily obtained

$$\delta\mathcal{C} \cdot \lambda = \begin{bmatrix} \dfrac{\delta\psi^k}{\delta\psi^l} \\ \dfrac{}{\delta\phi} \end{bmatrix}^T \cdot \begin{bmatrix} \lambda & (\underline{h}_{\alpha\alpha} \sin\phi + \underline{h}_{\alpha\beta} \cos\phi) \\ -\ \lambda & (\underline{h}_{\alpha\alpha} \sin\phi + \underline{h}_{\alpha\beta} \cos\phi) \\ \lambda & (g_{\alpha\alpha} \cos\phi - g_{\alpha\beta} \sin\phi) \end{bmatrix} = \begin{bmatrix} \dfrac{\delta\psi^k}{\delta\psi^l} \\ \dfrac{}{\delta\phi} \end{bmatrix}^T \cdot \underline{\mathcal{F}}^c. \tag{97}$$

Here again, these forces of constraint must be discretized so that the work they perform vanishes exactly. The following discretization is proposed

$$\underline{\mathcal{F}}^c_m = \begin{bmatrix} s\lambda_m & (\underline{h}_{\alpha\alpha m} \sin_m\phi + \underline{h}_{\alpha\beta m} \cos_m\phi) \\ -\ s\lambda_m & (\underline{h}_{\alpha\alpha m} \sin_m\phi + \underline{h}_{\alpha\beta m} \cos_m\phi) \\ s\lambda_m & (g_{\alpha\alpha m} \cos\phi_m - g_{\alpha\beta m} \sin\phi_m) \end{bmatrix}, \tag{98}$$

where $\sin_m\phi = (\sin\phi_f + \sin\phi_i)/2$ and $\sin\phi_m = \sin(\phi_f + \phi_i)/2$, with similar notations for the cosine function; and $g_{\alpha\beta m} = (g_{\alpha\beta f} + g_{\alpha\beta i})/2$. The work done by these forces is

$$\begin{aligned} \Delta\mathcal{W}^c = {} & s\lambda_m\ (\underline{r}^{kT} - \underline{r}^{lT})\ \left[\underline{h}_{\alpha\alpha m} \sin_m\phi + \underline{h}_{\alpha\beta m} \cos_m\phi\right] \\ & + s\lambda_m\ 2\sin\frac{\phi_f - \phi_i}{2} \left[g_{\alpha\alpha m} \cos\phi_m - g_{\alpha\beta m} \sin\phi_m\right]. \end{aligned} \tag{99}$$

Note that the increment in relative rotation was selected as $2\sin(\phi_f - \phi_i)/2$. The first term can be handled in the same manner as in eq. (95), and trigonometric identities are used to reduce the second term to find

$$\begin{aligned}\Delta\mathcal{W}^c &= s\lambda_m \ [(g_{\alpha\alpha f} - g_{\alpha\alpha i}) \ \sin_m \phi + (g_{\alpha\beta f} - g_{\alpha\beta i}) \ \cos_m \phi \\ &+ g_{\alpha\alpha m}(\sin\phi_f - \sin\phi_i) + g_{\alpha\beta m}(\cos\phi_f - \cos\phi_i)] \\ &= s\lambda_m \ (\mathcal{C}_f - \mathcal{C}_i). \end{aligned} \tag{100}$$

In summary, discretization (98) together with the constraint $\mathcal{C}_f = 0$ leads to the vanishing of the work done by the forces of constraint. Here again, this energy preserving formulation can be readily extended to an energy decaying formulation by following the steps outlined in section 4.3.

8 Time step size adaptation procedure

The response of constrained multi-body system often rapidly varies in time, prompting the need for an automated time step size adaptation procedure. The first step toward the development of such procedure is the choice of a measure of the error associated with the time discretization of the equations of motion. Within the framework of the energy decaying scheme, the following error measure e is proposed

$$e = \frac{\mathcal{E}^d}{\mathcal{E}_i}, \tag{101}$$

which corresponds to the amount of energy $\mathcal{E}^d$ dissipated by the scheme, normalized by the initial energy. For energy decaying schemes, the numerically dissipated energy $\mathcal{E}^d = c^2$ is a positive quantity, as shown in eq. (48). It is an integrated quantity that reflects errors in both velocities and strains at all points of the structure. Note that for the exact solution no numerical dissipation should take place and $e = 0$.

Consider, at first, the energy decaying discretization of the single degree of freedom, linear oscillator described in section 2.5. The error measure can be explicitly computed as

$$e = 1 - \rho^2 = \frac{(\omega\Delta t)^4}{(\omega\Delta t)^4 + 4(\omega\Delta t)^2 + 36}, \tag{102}$$

where ρ is the spectral radius of the amplification matrix. This relationship can be inverted to find

$$\omega\Delta t = \sqrt{2\ \frac{e + \sqrt{9e - 8e^2}}{1 - e}} \approx \sqrt{6}\sqrt[4]{e}, \tag{103}$$

which gives the time step size required to achieve a specified error level. It will be convenient to write this relationship in the following manner

$$\frac{\Delta t_{new}}{\Delta t_{old}} \approx \sqrt[4]{\frac{\hat{e}}{e_{old}}}, \tag{104}$$

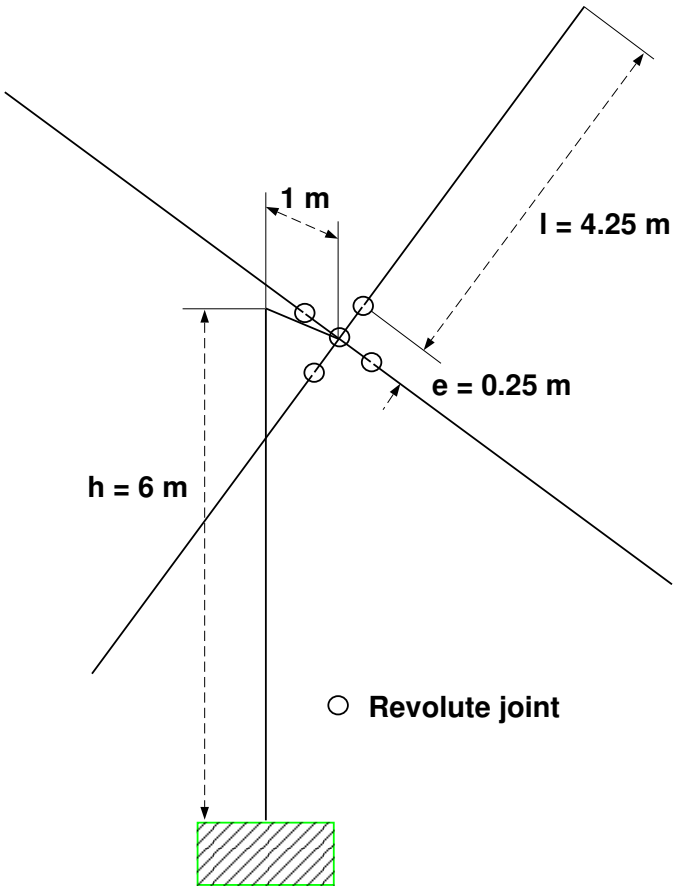

Figure 26: The windmill problem.

where Δt_{new} is the time step size that will achieve a desired error level $\hat{e}$, if a previous time step size Δt_{old} corresponded to an error level e_{old}.

We now turn to nonlinear, flexible multi-body systems. The error measure given by eq. (101) is still a rigorous error measure for such system since no numerical dissipation occurs in the exact solution. However, the relationship between the error measure and the time step is no longer given by eq. (102). Nevertheless, the time step size update formula of eq. (104) was found to be a reliable estimate of the time step size required to achieve a desired level of accuracy in complex multi-body systems.

9 Numerical Examples

9.1 The windmill resonance problem

The first example deals the windmill resonance problem depicted in fig. 26 and will be used to illustrate the different behavior of the energy preserving and decaying schemes. Consider a four-bladed rotor mounted on an elastic tower. The tower has a height $h = 6.0\ m$, bending stiffnesses $I_{22} = I_{33} = 3.87\ MN.m^2$, a torsional stiffness $GJ = 2.97\ MN.m^2$, and a mass

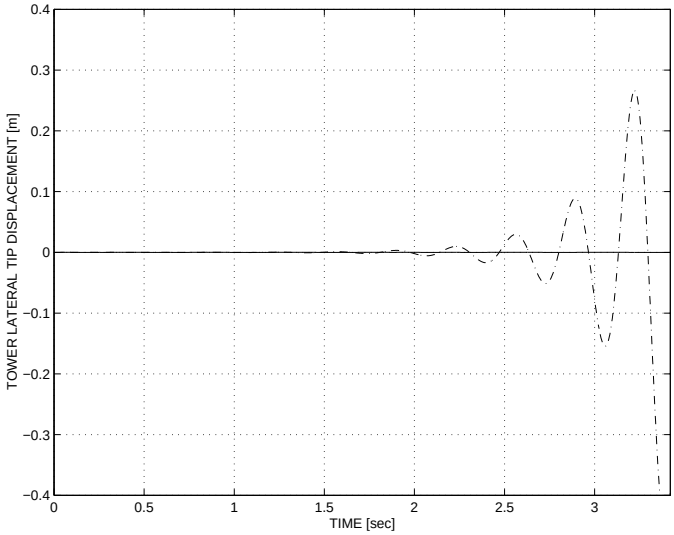

Figure 27: Time history of the tower tip lateral deflection for two rotor speed $\Omega = 15\ rad/sec$ (solid line), and 30 rad/sec (dashed line).

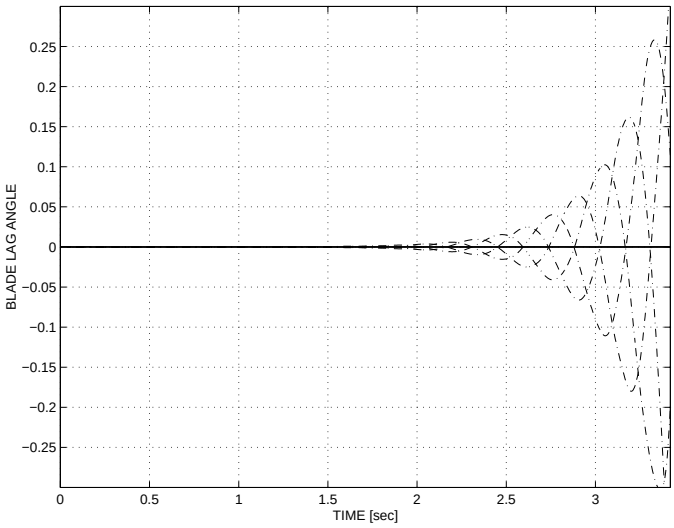

Figure 28: Time history of the lag angles for the four blades for two rotor speed $\Omega = 15\ rad/sec$ (solid line), and 30 rad/sec (dashed line).

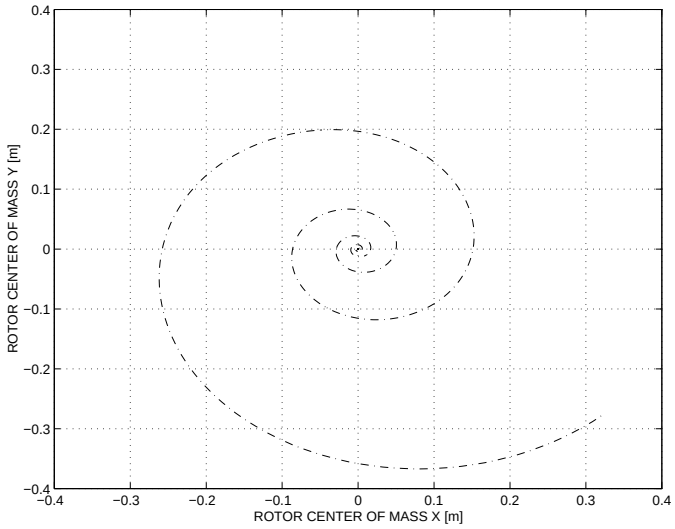

Figure 29: Time history of the location of the rotor center of mass for two rotor speed $\Omega = 15\ rad/sec$ (solid line), and 30 rad/sec (dashed line).

per unit span $m_T = 12.72\ kg/m$. A 30 kg concentrated mass is located at the top of the tower. A nacelle is connected to the tip of the tower and projects 1.0 m forward. The nacelle properties are identical to those of the tower. The rotor hub is located at the tip of the nacelle and is represented by a 20 kg concentrated mass. Each blade is uniform and has a length $l = 4.25\ m$, a mass $m_b = 12.75\ kg$, in- and out-of-plane bending stiffness of $I_{33} = 4.71\ kN.m^2$, and $I_{22} = 0.547\ kN.m^2$, respectively, and the blade's hinge located at distance $e = 0.25\ m$ from the hub. The tower and nacelle are discretized with two and one cubic beam elements, respectively, whereas each blade is discretized with three cubic beam elements. A revolute joint located at the tip of the nacelle allows rotation of the rotor, and four revolute joints model the four lead-lag hinges of the blades.

At first, two cases will be studied with initial rotor speeds $\Omega = 15\ rad/sec$ and 30 rad/sec, which correspond to stable, and unstable rotor speeds, respectively. Fig. 27 shows the time history of the tower tip lateral deflection. The lower rotor speed is in the stable operation range, whereas the higher speed is in the unstable range. Fig. 28 shows the corresponding lag angles for the four blades of the rotor. The exponential growth of these quantities clearly demonstrate the catastrophic effect of the unstable behavior of the system. The mechanism triggering this instability is better understood by looking at the time history of the location of the rotor center of mass as viewed by an inertial observer, as depicted in fig. 29. As the instability sets in, the rotor's center of mass spirals around as a result of the blade's lag motion. This motion excites the tower at its natural frequency and initiates the instability.

Next, the behavior of the system will be studied under the effect of a constant torque $T = 500\ M.m$ applied at the rotor hub. The rotor is initially rotating at a constant angular velocity $\Omega = 15\ rad/sec$, *i.e.* in the stable regime. At that instant, the constant torque is applied and the rotor speed increases, driving the system into an unstable regime. The sudden application of the hub torque excites high frequency vibrations in both tower and

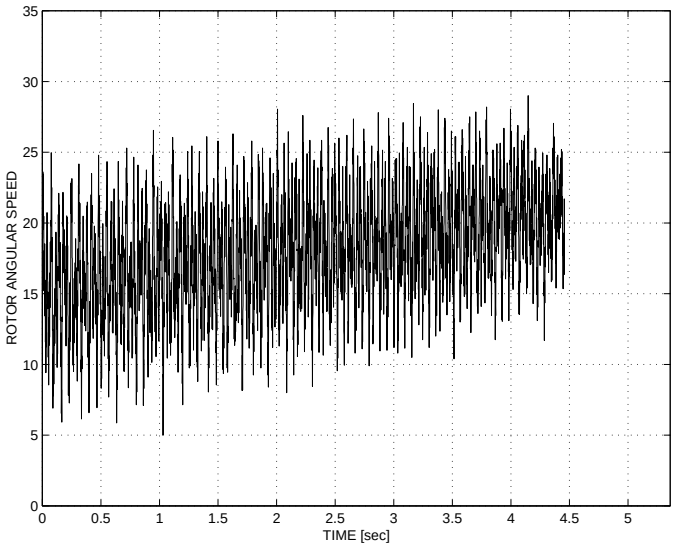

Figure 30: Time history of the rotor speed under the effect of an applied hub torque, using the energy preserving scheme.

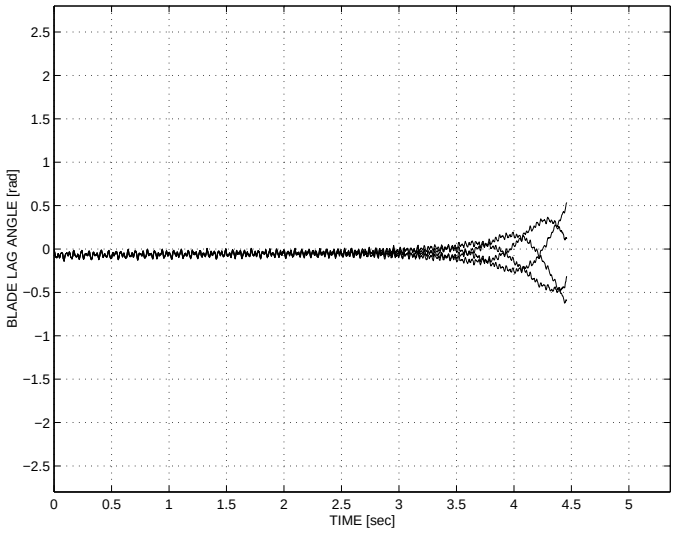

Figure 31: Time history of the lag angles for the four blades under the effect of an applied hub torque, using the energy preserving scheme.

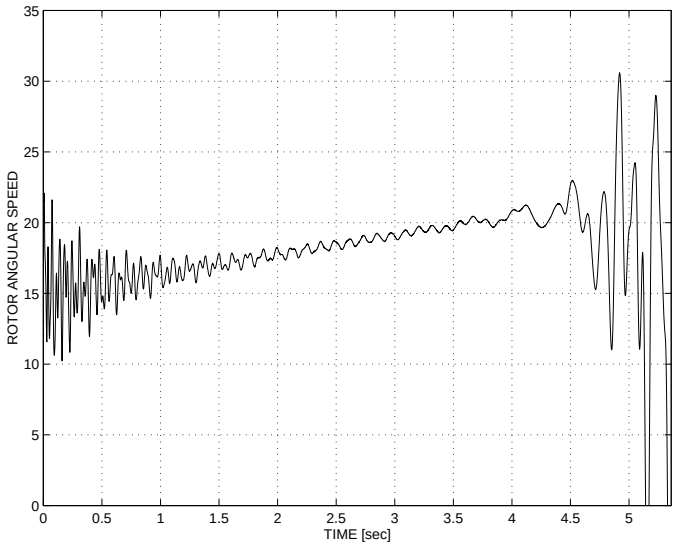

Figure 32: Time history of the rotor speed under the effect of an applied hub torque, using the energy decaying scheme.

rotor. First, this problem is treated with the energy preserving scheme. Fig. 30 shows the increasing rotor speed due to the applied torque. However, very high frequency vibrations are superposed to the slow rise in rotor speed. Since no physical damping is present in the system, and no numerical dissipation is provided by the energy preserving scheme, these oscillations do not damp out. The same phenomenon is observed in fig. 31 for the lag angles of the four blades. The presence of these high frequencies hinders the convergence process at each time step, and requires an increasing number of iterations to be used. At time $t = 4.466$ *sec*, convergence fails, and the simulation is terminated.

On the other hand, fig. 32 shows the results of the simulation of the same problem using the energy decaying scheme. Though high frequency oscillations are present at the beginning of the simulation due to the sudden application of the hub torque, the energy decaying scheme now provides high frequency numerical dissipation that rapidly damps out the energy associated with the high frequency vibrations. Typically, 4 iterations are required at each time step, as compared to 7 with the use of the energy preserving scheme. Furthermore, the simulation can proceed for a longer period of time, up to $t = 5.36$ *sec* as depicted in fig. 33. By that time, very large blade angular motions are observed, and the exponential growth gives place to a limit cycle type behavior involving complex blade motions.

9.2 The four bar mechanism problem

The second problem deals with a four bar mechanism problem depicted in fig. 34 and is used to demonstrate the automated time step size selection procedure described in section 8. Bar 1 is of length $L_1 = 0.12$ m and is connected to the ground at point A by means of a revolute joint. Bar 2 is of length $L_2 = 0.24$ m and is connected to bar 1 at point B

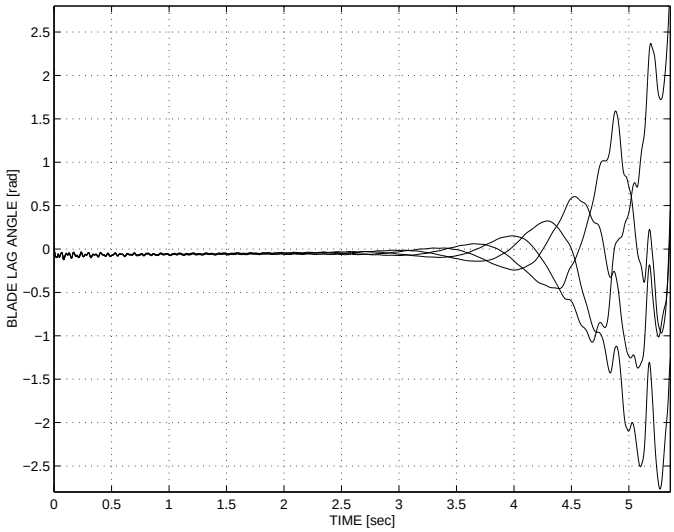

Figure 33: Time history of the lag angles for the four blades under the effect of an applied hub torque, using the energy decaying scheme.

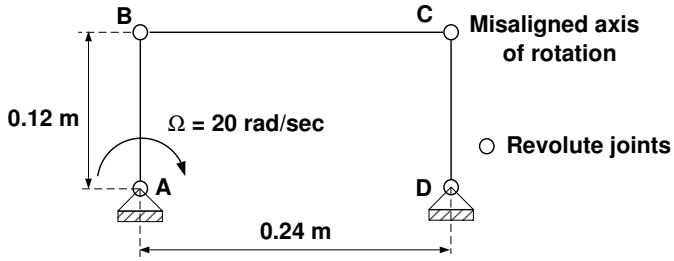

Figure 34: The four bar mechanism problem.

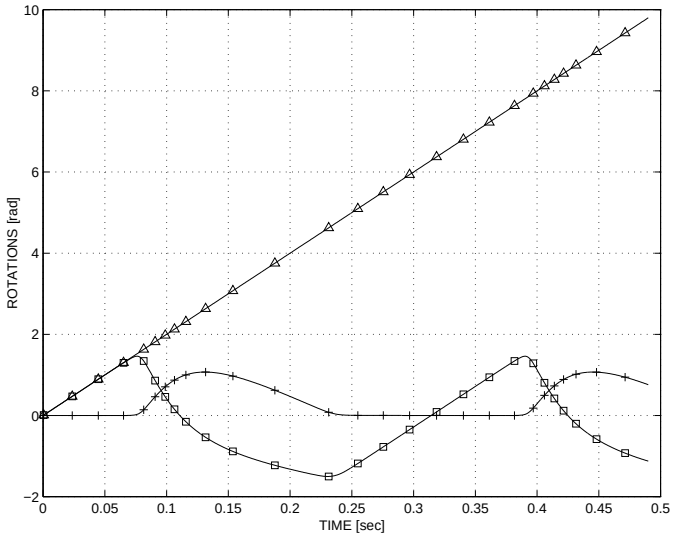

Figure 35: Time history of rotations of the system. Relative rotations at points A ($\triangle$) and D ($\square$), and absolute rotation of bar 2 ($+$).

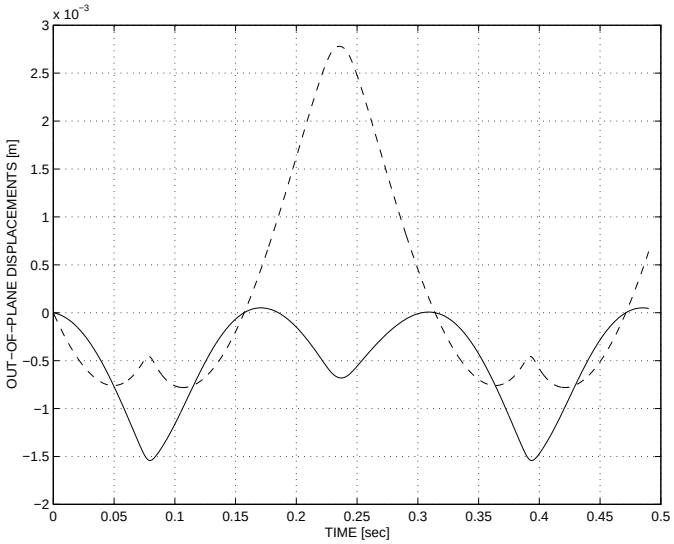

Figure 36: Time history of out-of-plane displacements at points B (solid line) and C (dashed line).

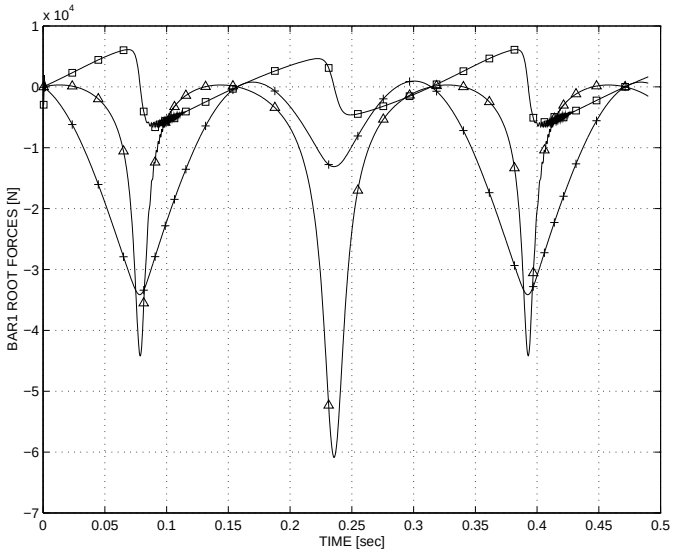

Figure 37: Time history of forces at the root of bar 1, in local axes. Axial forces ($\triangle$), in-plane shear forces ($\square$), and out-of-plane shear force ($+$).

with a revolute joint. Finally, bar 3 is of length $L_3 = 0.12\ m$ and is connected to bar 2 and the ground at points C and D, respectively, by means of two revolute joints. In the reference configuration the bars of this planar mechanism intersect each other at 90 degree angles and the axes of rotation the revolute joints at points A, B, and D are normal to the plane of the mechanism. However, the axis of rotation the revolute joint at point C is at a 5 degree angle with respect to this normal to simulate an initial defect in the mechanism. A torque is applied on bar 1 at point A so as to enforce a constant angular velocity $\Omega = 20\ rad/sec$. If the bars were infinitely rigid, no motion would be possible as the mechanism locks. For elastic bars, motion becomes possible, but generates large internal forces. Bar 1 has the following physical characteristics: axial stiffness $EA = 40\ MN$, bending stiffnesses $EI_{22} = EI_{33} = 0.24\ MN.m^2$, torsional stiffness $GJ = 0.28\ MN.m^2$, and mass per unit span $m = 3.2\ kg/m$. Bars 2 and 3 have the following physical characteristics: axial stiffness $EA = 40\ MN$, bending stiffnesses $EI_{22} = EI_{33} = 24\ kN.m^2$, torsional stiffness $GJ = 28\ kN.m^2$, and mass per unit span $m = 1.6\ kg/m$.

If the four revolute joints had their axes of rotation orthogonal to the plane of the mechanism, the response of the system would be purely planar, and bars 1 and 3 would rotate at constant angular velocities around points A and D, respectively. The initial defect in the mechanism causes a markedly different response. Fig. 35 shows the time history of the relative rotations at points A and D, as well the absolute rotation of the mid point of bar 2. Bar 1 rotates at a constant angular velocity under the effect of the applied torque, but bar 3 now oscillates back and forth, never completing an entire turn. When the direction of rotation of bar 3 reverses, bar 2 undergoes large rotations, instead of near translation. Furthermore, the response is three dimensional as shown in fig. 36 which depicts the time history of out-of-plane displacements at points B and C. Point C undergoes a 3 mm maximum out-of-plane displacement.

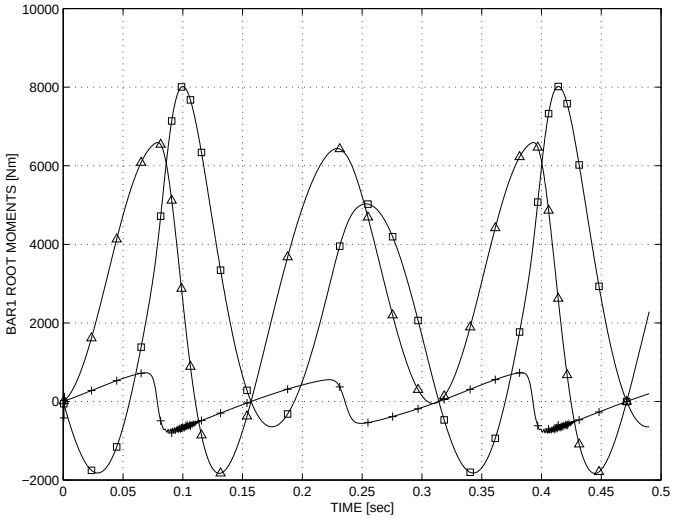

Figure 38: Time history of moments at the root of bar 1, in local axes. Torque (△), in-plane bending moment (□), and out-of-plane bending moment (+).

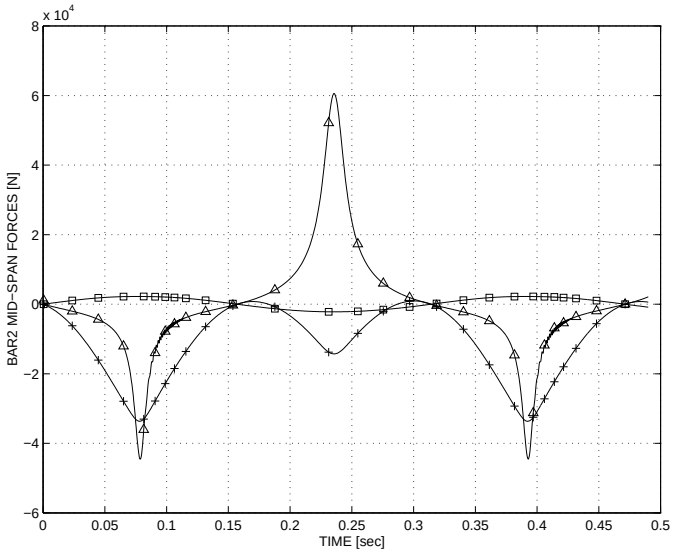

Figure 39: Time history of forces at mid-span of bar 2, in local axes. Axial forces (△), in-plane shear forces (□), and out-of-plane shear force (+).

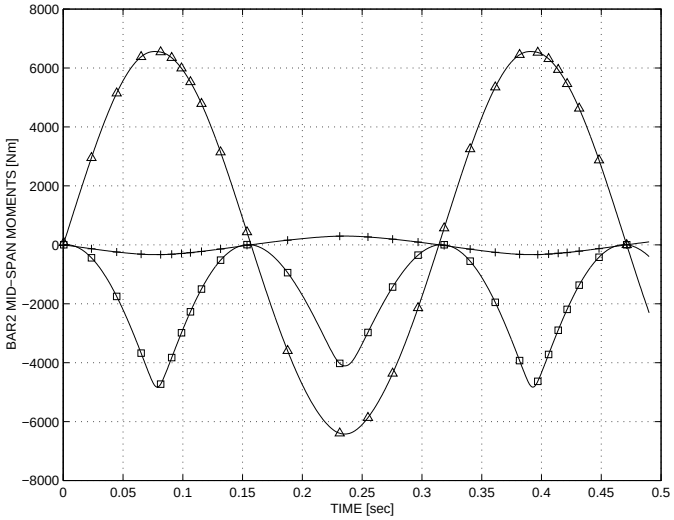

Figure 40: Time history of moments at mid-span of bar 2, in local axes. Torque ($\triangle$), in-plane bending moment ($\square$), and out-of-plane bending moment ($+$).

The time history of the three components of the internal force at the root of bar 1 are shown in fig. 37, whereas fig. 38 shows the time history of components of twisting and bending moments at the same location. The corresponding quantities at mid-span of bar 2 are shown in figs 39 and 40. These large internal forces are all caused by the initial imperfection of the mechanism.

For this problem, the automated time step size selection procedure described in section 8 was used. Fig. 41 shows the time history of the time step size which varied as much as by a factor of six during the simulation. The desired local error level, as defined by eq. (101), was set to be $\hat{e} = 1.0 \times 10^{-06}$ and a new time step size was evaluated at each time step according to eq. (104). Fig. 42 shows the time history of the cumulative error measure obtained by summing the error at each time step. This result shows that less than 0.013% error was accumulated over the entire simulation.

9.3 The tail rotor transmission problem

The last problem deals with the supercritical transmission of a helicopter tail rotor. Fig. 43 shows the configuration of the problem. The aft part of the helicopter is modeled and consists of a 6 m fuselage section which connects at a 45 degree angle to a 1.2 m projected length tail section. This structure supports the transmission to which it is connected at points M and T by means of 0.25 m support brackets. The transmission is broken into two shafts, each connected to flexible joints at either end. Shaft 1 is connected to a revolute joint at point S, and gear box 1 at point G. Shaft 2 is connected to gear box 1 and gear box 2 which transmits power to the tail rotor with its axis of rotation normal to the plane of the drawing. The gear ratios in gear boxes 1 and 2 are 1:1 and 2:1, respectively.

The fuselage has the following physical characteristics: axial stiffness $EA = 687\ MN$, bending stiffnesses $EI_{22} = 19.2\ MN.m^2$, $EI_{33} = 26.9\ MN.m^2$, torsional stiffness $GJ =$

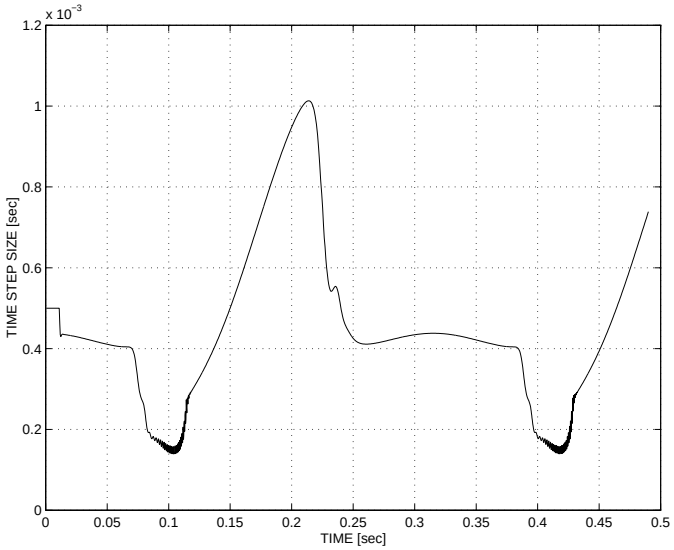

Figure 41: Time history of the time step size.

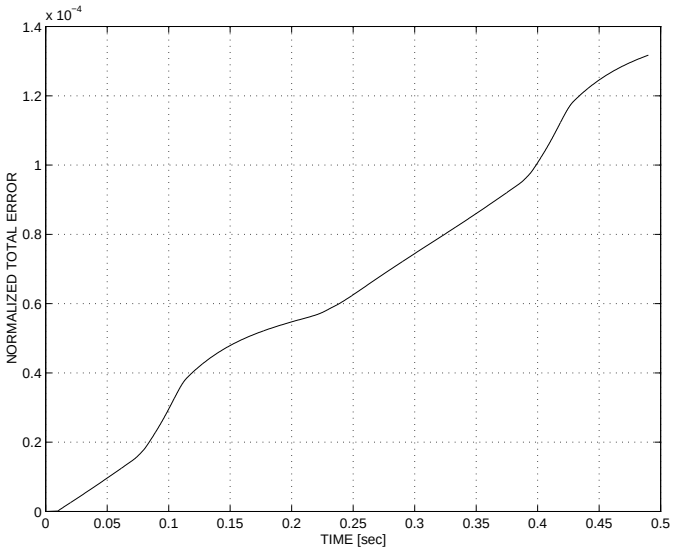

Figure 42: Time history of the cumulative error measure.

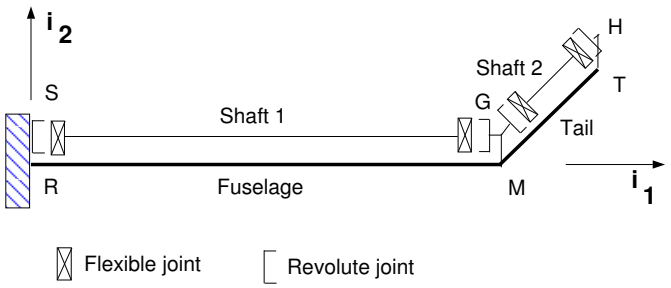

Figure 43: Configuration of the tail rotor transmission problem.

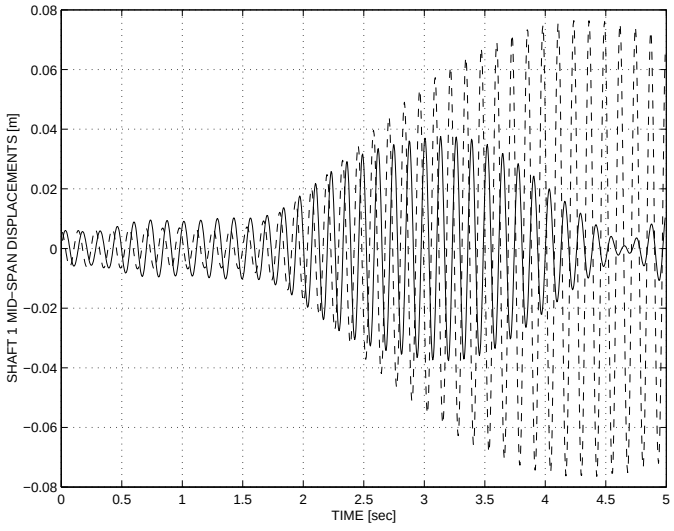

Figure 44: Time history of shaft 1 mid-span transverse deflections. u_2: dashed line; u_3: solid line.

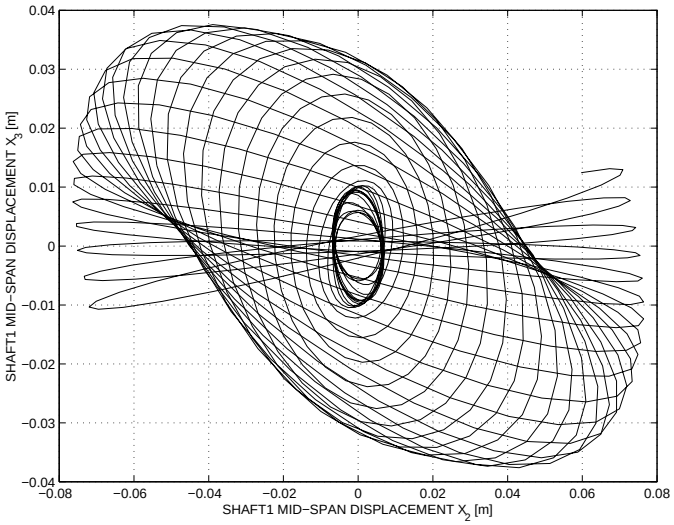

Figure 45: Motion of shaft 1 mid-span point projected onto the $\vec{\imath}_2$, $\vec{\imath}_3$ plane.

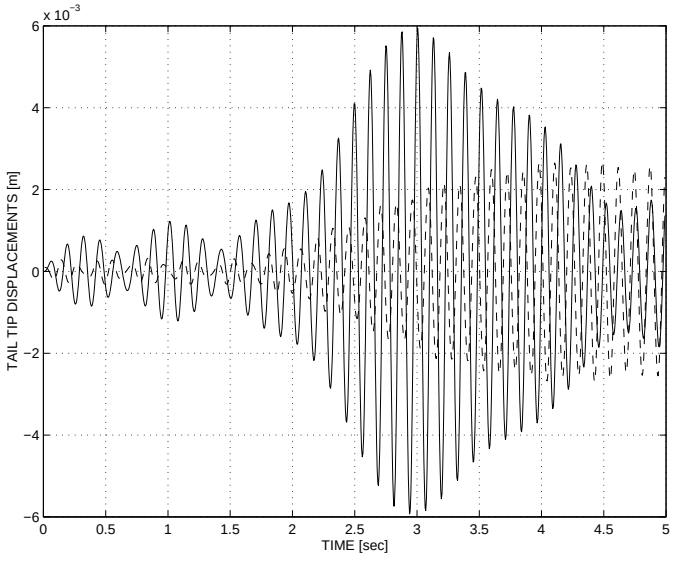

Figure 46: Time history of tail tip transverse displacements. u_2: dashed line; u_3: solid line.

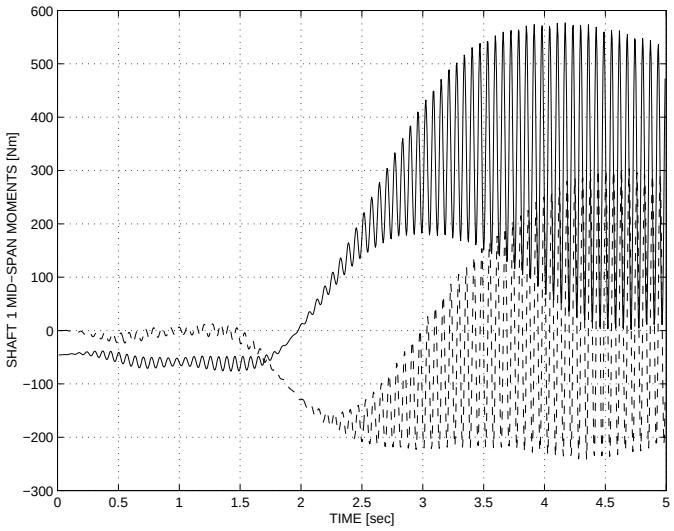

Figure 47: Time history of shaft 1 mid-span bending moments in local axes. M_2: dashed line; M_3: solid line.

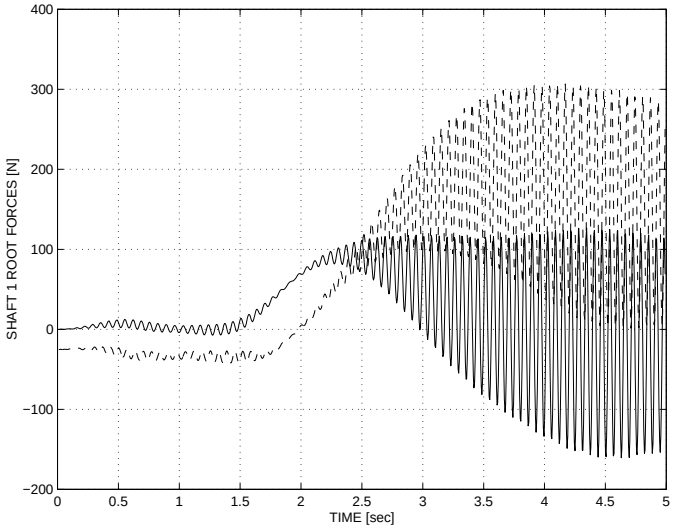

Figure 48: Time history of shaft 1 root forces in local axes. F_2: dashed line; F_3: solid line.

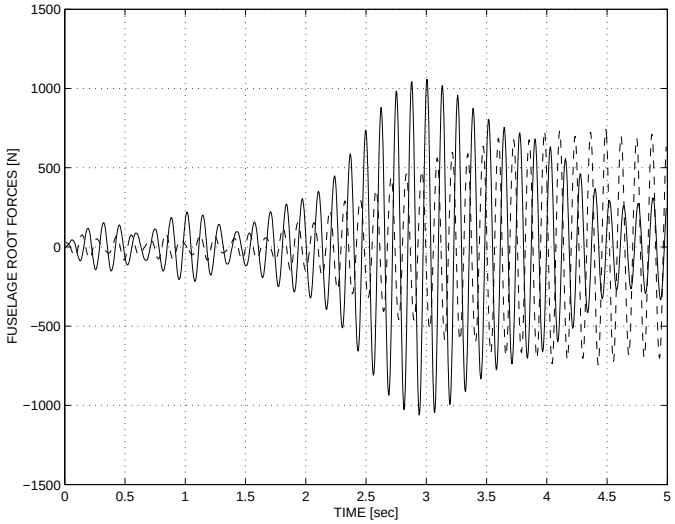

Figure 49: Time history of fuselage root forces in local axes. F_2: dashed line; F_3: solid line.

8.77 $MN.m^2$, and mass per unit span $m = 15.65\ kg/m$. The properties of the tail are one third of those of the fuselage. Shafts 1 and 2 have the following physical characteristics: axial stiffness $EA = 22.9\ MN$, bending stiffnesses $EI_{22} = 26.7\ kN.m^2$ and $EI_{33} = 27.7\ kN.m^2$, torsional stiffness $GJ = 22.1\ kN.m^2$, and mass per unit span $m = 0.848\ kg/m$. The center of mass of the shaft has a 1 mm offset with respect to the shaft reference line. The small difference in bending stiffnesses together with the center of mass offset are meant to represent an initial manufacturing imperfection or an unbalance in the shaft. The stiffness properties of the flexible couplings are as follows: axial stiffness 5.0 kN/m, transverse stiffnesses 1.0 MN/m, torsional stiffness 0.1 $MN.m/rad$, and bending stiffnesses 0.1 $kN.m/rad$. Finally, gear boxes 1 and 2 have a concentrated mass of 5.0 kg each, and the tail rotor a 15.0 kg mass with a polar moment of inertia of 3.0 $kg.m^2$.

The lowest two natural frequencies of shaft 1 were found to be $\omega_1 = 47.5$ and $\omega_2 = 49.1\ rad/sec$. According to linear theory, the system is stable when the shaft angular velocity is below ω_1 or above ω_2, but unstable between theses two speeds. The initial condition of the simulation was selected as the static equilibrium configuration of the system when shafts 1 and 2 are rotating at an angular velocity $\Omega = 45\ rad/sec$. A torque Q is applied to shaft 1 at point S and has the following time history

$$\begin{aligned} Q(t) &= 0 && t < 1\ sec \\ &= 8\ (1 - cos\ 2\pi t) && 1 < t < 2\ sec \\ &= 0 && t > 2\ sec. \end{aligned} \tag{105}$$

As a result, shaft 1 which is initially operating in a stable regime ($\Omega = 45\ rad/sec$) accelerates and is forced to operate through the critical speed range. The simulation was run with a constant time step $\Delta t = 5 \times 10^{-04}\ sec$ for a total time of 5 sec, corresponding to about 40 revolutions of shaft 1. Fig. 44 shows the time history of shaft 1 mid-span transverse deflections. Up to about 1.6 sec into the simulation, the response remains small. At that

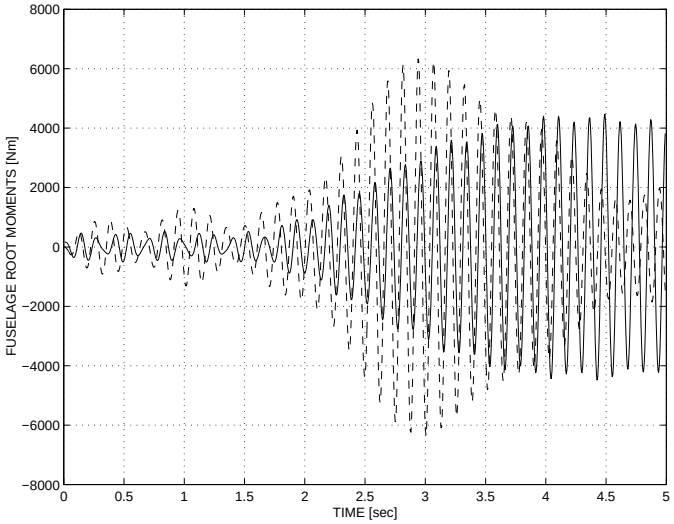

Figure 50: Time history of fuselage root bending moments in local axes. M_2: dashed line; M_3: solid line.

point, the shaft angular velocity increases due to the applied torque, and a linear growth in transverse displacement amplitude is observed as expected in the critical speed zone. As the shaft angular velocity continues to increase, the unstable zone is crossed and response amplitudes level off. The motion of the shaft mid-span point projected onto the $\vec{i}_2$, $\vec{i}_3$ plane is depicted in fig. 45 which shows the whirling motion associated with the crossing of the critical speed zone. Of course, shaft 1 motions induce vibrations in the fuselage as shown in fig. 46 which depicts the time history of tail tip transverse displacements.

The large amplitude vibrations of shaft 1 during the crossing of the critical speed zone generate significant mid-span bending moments and root forces, both measured a body attached coordinate system, that are depicted in figs. 47 and 48, respectively. Of course, these vibrations induce large loads at the fuselage root section; figs. 49 and 50 show the root forces and bending moments, respectively.

All the results described here were obtained the energy decaying scheme. Fig. 51 shows the time history of the cumulative error measure obtained by summing the error at each time step; less than 0.0002% error was accumulated during the entire 10,000 step simulation.

10 Conclusions

In this paper, two novel time integration schemes for flexible, nonlinear multi-body systems were presented. First, the energy preserving scheme which combines two features: an energy preservation statement for the elastic bodies, and the vanishing of the work done by the forces of constraint. This results in exact preservation of the total energy for the nonlinear multi-body system and *unconditional stability* is achieved. The scheme presents second order accuracy and has no numerical dissipation.

Second, the energy decaying scheme combines two features: an energy decay inequality

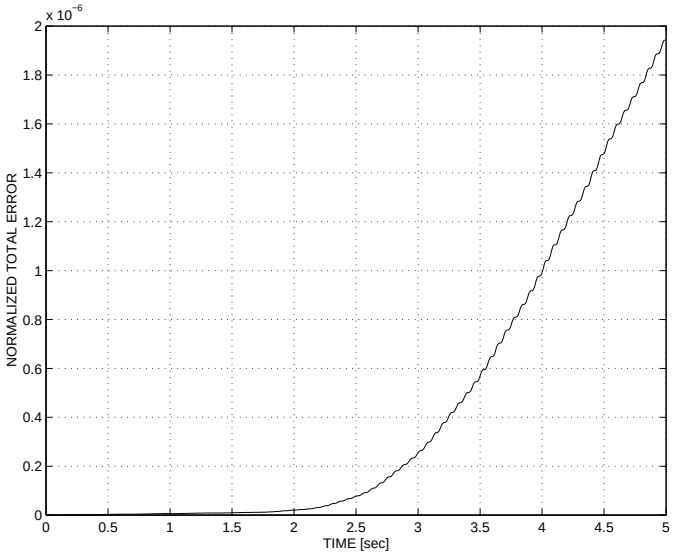

Figure 51: Time history of the cumulative error measure.

for the elastic bodies, and the vanishing work done by the forces of constraint. This results in the decay of the total energy of the multi-body system and *unconditional stability* is achieved. This scheme presents third order accuracy and high frequency numerical dissipation.

Simple numerical examples have been presented to illustrate the proposed integration schemes. The energy decaying scheme clearly provides the unconditional stability and high frequency numerical dissipation characteristics required for the analysis of flexible, nonlinear multi-body problems.

The formulation and discretization of specific elements were presented. The discretizations of the inertial and elastic forces associated with beam and flexible joint elements were described in detail, as well as the discretizations of the constraint forces associated with universal and revolute joints. Finally, an automated time step size selection procedure was presented that uses an error measure based on the amount of energy dissipated in the numerical scheme. Both local and global error levels can be evaluated in complex simulations.

A number of simulations of realistic multi-body systems were presented that illustrate the versatility and accuracy of the proposed schemes, and demonstrate the need for unconditional stability and high frequency numerical dissipation.

References

[1] T.J.R. Hughes. Analysis of transient algorithms with particular reference to stability behavior. In T. Belytschko and T.J.R. Hughes, editors, *Computational Methods for Transient Analysis*, pages 67–155. North-Holland, Amsterdam, 1983.

[2] N.M. Newmark. A method of computation for structural dynamics. *Journal of the Engineering Mechanics Division*, 85:67–94, 1959.

[3] T.J.R. Hughes. *The Finite Element Method*. Prentice Hall, Inc., Englewood Cliffs, New Jersey, 1992.

[4] H.M. Hilber, T.J.R. Hughes, and R.L. Taylor. Improved numerical dissipation for time integration algorithms in structural dynamics. *Earthquake Engineering and Structural Dynamics*, 5:282–292, 1977.

[5] J. Chung and G.M. Hulbert. A time integration algorithm for structural dynamics with improved numerical dissipation: The generalized-α method. *Journal of Applied Mechanics*, 60:371–375, 1993.

[6] J.C. Simo and K. Wong. Unconditionally stable algorithms for rigid body dynamics that exactly preserve energy and momentum. *International Journal for Numerical Methods in Engineering*, 31:19–52, 1991.

[7] J.C. Simo and N. Tarnow. The discrete energy-momentum method. Conserving algorithms for nonlinear dynamics. *ZAMP*, 43:757–792, 1992.

[8] J.C. Simo, N. Tarnow, and M. Doblare. Non-linear dynamics of three-dimensional rods: Exact energy and momentum conserving algorithms. *International Journal for Numerical Methods in Engineering*, 38:1431–1473, 1995.

[9] O.A. Bauchau, G. Damilano, and N.J. Theron. Numerical integration of nonlinear elastic multi-body systems. *International Journal for Numerical Methods in Engineering*, 38:2727–2751, 1995.

[10] C. Johnson. *Numerical Solutions of Partial Differential Equations by the Finite Element Method*. Cambridge University Press, Cambridge, 1987.

[11] C. Johnson, U. Nävert, and V. Pitkäranta. Finite element methods for linear hyperbolic problems. *Computer Methods in Applied Mechanics and Engineering*, 45:285–312, 1984.

[12] C. Johnson and V. Szepessy. Convergence of a finite element method for a nonlinear hyperbolic conservation law. Technical Report 1985-25, Mathematics Department, Chalmers University of Technology, Göteborg, Sweden, 1985.

[13] T.R.J. Hughes and M. Hulbert. Space-time finite element formulations for elastodynamics: Formulation and error estimates. *Computer Methods in Applied Mechanics and Engineering*, 66:339–363, 1988.

[14] M. Hulbert. *Space-Time Finite Element Methods for Second-Order Hyperbolic Equations*. PhD thesis, Stanford University, 1989.

[15] O.A. Bauchau and N.J. Theron. Energy decaying scheme for non-linear beam models. *Computer Methods in Applied Mechanics and Engineering*, 134:37–56, 1996.

[16] O.A. Bauchau and T. Joo. Computational schemes for nonlinear elasto-dynamics. *International Journal for Numerical Methods in Engineering*, 45:693–719, 1999.

[17] O.A. Bauchau and N.J. Theron. Energy decaying schemes for nonlinear elastic multi-body systems. *Computers and Structures*, 59:317–331, 1996.

[18] C.L. Bottasso and M. Borri. Energy preserving/decaying schemes for non-linear beam dynamics using the helicoidal approximation. *Computer Methods in Applied Mechanics and Engineering*, 143:393–415, 1997.

[19] C.L. Bottasso and M. Borri. Integrating finite rotations. *Computer Methods in Applied Mechanics and Engineering*, 164:307–331, 1998.

[20] C.L. Bottasso, M. Borri, and L. Trainelli. Integration of elastic multibody systems by invariant conserving/dissipating algorithms. Part I: formulation. *Computer Methods in Applied Mechanics and Engineering*, 190:3669–3699, 2001.

[21] C.L. Bottasso, M. Borri, and L. Trainelli. Integration of elastic multibody systems by invariant conserving/dissipating algorithms. Part II: numerical schemes and applications. *Computer Methods in Applied Mechanics and Engineering*, 190:3701–3733, 2001.

[22] C. Lanczos. *The Variational Principles of Mechanics*. Dover Publications, Inc., New York, 1970.

[23] T.R. Kane and D.A. Levinson. *Dynamics: Theory and Applications*. McGraw-Hill, Inc., New York, 1985.

Appendix A Rodrigues parameters

A common representation of finite rotations [23] is in terms of Rodrigues parameters $\underline{r} = 2\underline{u}\ \tan\phi/2$, where ϕ is the magnitude of the finite rotation and $\underline{u}$ the components of the unit vector about which it takes place. The following notation is introduced

$$r_0 = \cos^2\frac{\phi}{2} = 1\ /\ (1 + \frac{\underline{r}^T\ \underline{r}}{4}). \tag{A1}$$

The finite rotation tensor R, and the rotation tensor G corresponding to a finite rotation of magnitude $\phi/2$ about the same axis write

$$R(\underline{r}) = I + r_0\ \widetilde{r} + \frac{r_0}{2}\ \widetilde{r}\widetilde{r};\quad G(\underline{r}) = I + \frac{\sqrt{r_0}}{2}\ \widetilde{r} + \frac{r_0}{4(1+\sqrt{r_0})}\ \widetilde{r}\widetilde{r}. \tag{A2}$$

The relationship between angular velocities $\underline{\omega}$ and time derivatives of Rodrigues parameters is $\underline{\omega} = H\ \dot{\underline{r}}$, where

$$H(\underline{r}) = r_0(1 + \frac{1}{2}\ \widetilde{r}). \tag{A3}$$

These operators enjoy the following properties

$$RR^T = I;\quad R\underline{r} = \underline{r};\quad GG^T = I;\quad G\underline{r} = \underline{r};\quad R = GG. \tag{A4}$$

$$\widetilde{r}\ \frac{G+G^T}{2} = \frac{G+G^T}{2}\ \widetilde{r} = G - G^T. \tag{A5}$$

$$\left(I - \frac{\widetilde{r}}{2}\right) G = \left(I + \frac{\widetilde{r}}{2}\right) G^T = \left(\frac{G+G^T}{2}\right)^{-1}. \tag{A6}$$

Appendix B Discretization of finite rotations

Let R_i R_f be the components of the rotation tensor $\mathbf{R}$ at times t_i and t_f, respectively. The incremental rotation $R = R_f R_i^T$ can be divided in two equal parts such that $R = GG$. In this work, the incremental rotation is parameterized with Rodrigues parameters $\underline{r}$. The expressions for $R(\underline{r})$ and $G(\underline{r})$ are given in Appendix A. A mid-point rotation is now easily defined as $R_m = GR_i$. The following relationships summarize the properties of the discretization of the finite rotations

$$\begin{array}{lll} G = R_m R_i^T & G = R_f R_m^T & R = R_f R_i^T \\ G^* = R_0^T R_i^T R_m R_0 & G^* = R_0^T R_m^T R_f R_0 & R^* = R_0^T R_m^T R_f R_i^T R_m R_0. \end{array} \tag{B1}$$

The following operator are extensively used

$$R_a = \frac{R_f + R_i}{2}; \quad \mathcal{R}_a = \begin{bmatrix} R_a & 0 \\ 0 & R_a \end{bmatrix}; \quad \mathcal{R}_b = \begin{bmatrix} R_a & 0 \\ 0 & HG^T R_m R_0 \end{bmatrix}. \tag{B2}$$